https://doi.org/10.5194/tc-2021-80
Preprint. Discussion started: 8 April 2021
© Author(s) 2021. CC BY 4.0 License.

The Cryosphere Discussions

The MOSAiC Drift: Ice conditions from space and comparison with previous years

Thomas Krumpen[1*], Luisa von Albedyll[1*], Helge F. Goessling[1*], Stefan Hendricks[1*], Bennet Juhls[1*], Gunnar Spreen[2*], Sascha Willmes[3*], H. Jakob Belter[1], Klaus Dethloff[1], Christian Haas[1], Lars Kaleschke[1], Christian Katlein[1], Xiangshan Tian-Kunze[1], Robert Ricker[1], Philip Rostosky[2], Janna Rueckert[2], Suman Singha[4], Julia Sokolova[5]

*These authors contributed equally to this work

[1]Alfred Wegener Institute, Helmholtz Centre for Polar and Marine Research, Am Handelshafen 12, 27570 Bremerhaven, Germany
[2]University of Bremen, Institute of Environmental Physics, Otto-Hahn Allee 1, 28359 Bremen, Germany
[3]University of Trier, Environmental Meteorology, Universitätsring 15, 54296 Trier, Germany
[4]German Aerospace Center, Remote Sensing Technology Institute, SAR Signal Processing, Am Fallturm 9, 28359 Bremen, Germany
[5]Arctic and Antarctic Research Institute, Ulitsa Beringa, 38, Saint Petersburg, 199397, Russia

Correspondence to: Thomas Krumpen (tkrumpen@awi.de)

Abstract.

We combine satellite data products to provide a first and general overview of the sea-ice conditions along the MOSAiC drift and a comparison with previous years. We find that the MOSAiC drift was around 25% faster than the climatological mean drift, as a consequence of large-scale low-pressure anomalies prevailing around the Barents-Kara-Laptev Sea region between January and March. In winter (October - April), satellite observations show that the sea-ice in the vicinity of the Central Observatory (CO) was rather thin compared to the previous years along the same trajectory. Unlike ice thickness, satellite-derived sea-ice concentration, lead frequency, and snow thickness during winter month were close to the long-term mean with little variability. With the onset of spring and decreasing distance to Fram Strait, variability in ice concentration and lead activity increased. In addition, frequency and strength of deformation events (divergence and shear) were higher during summer than during winter. Overall, we find that sea-ice conditions observed close (~ 5 km) to the CO are representative for the wider (50 km and 100 km) surroundings. An exception is the ice thickness: Here we find that sea-ice near the CO (50 km radius) was 4% thinner than sea-ice within a 100 km radius. Moreover, satellite acquisitions indicate that the formation of large melt ponds began earlier on the MOSAiC floe than on neighbouring floes.

https://doi.org/10.5194/tc-2021-80
Preprint. Discussion started: 8 April 2021
© Author(s) 2021. CC BY 4.0 License.

The Cryosphere Discussions

1 Introduction

In October 2019, the icebreaker *Polarstern* operated by the Alfred Wegener Institute Helmholtz Centre for Polar and Marine Research (AWI, 2017), was moored to an ice floe north of the Laptev Sea (October 4 at 85°N, 136°E). Scientists from 16 different nations onboard of *Polarstern* embarked on a one-year long journey along the Transpolar Drift towards Fram Strait (Fig. 1). The goal of the international Multidisciplinary drifting Observatory for the Study of Arctic Climate (MOSAiC) project is to better understand and quantify relevant processes within the atmosphere-ice-ocean coupled system and ecological and biogeochemical feedbacks, ultimately leading to much improved climate and Earth System models. The Central Observatory (CO) with comprehensive instrumentation was setup on the main floe; an ice floe measuring roughly 2.8 km × 3.8 km. The floe was part of a loose assembly of pack ice, less than a year old, which had survived the 2019 summer melt season (Krumpen et al., 2020). Around the CO, a distributed network (DN) of autonomous buoys was installed in a 40 km radius on 55 additional residual ice floes of similar age (Krumpen and Sokolov, 2020).

Ice conditions found on site at the start of the drift experiment were exceptional to begin with: Record temperatures in summer and strong offshore-directed ice drift in winter resulted in the second longest ice-free summer period since reliable instrumental records began. As a result, ice thickness was unusually thin compared to the previous 26 years (Krumpen et al., 2020). However, by the time the MOSAiC floe reached Fram Strait (around 300 days later), it had grown to a thickness typical for the region in summer in the past decade (results from IceBird airborne surveys, Fig. 1 in Belter et al. 2020).

Satellite data played a decisive role for the campaign. Using a combination of satellite images acquired prior to the start, Krumpen et al. (2020) were able to extend the MOSAiC expedition back in time by following the ice floe to its place of origin, the shallow shelf of the New Siberian Islands (Fig. 1). During the drift itself, satellite images were continuously taken over the ship and the extended surroundings to support scientific objectives and logistic needs. In this manuscript we make use of satellite data records collected along the drift track to categorize the different ice conditions and most prominent events that shaped and characterized the floe and surroundings from October 4, 2019 to July 31, 2020. A comparison with previous years is made whenever possible for the reference period 2005/2006 – 2018/2019. The aim of this analysis is to provide a very first and general overview of on-site conditions for upcoming physical, biogeochemical and ecological MOSAiC studies.

Below, we introduce the different satellite products used to describe the sea-ice conditions along the drift. A short description of the large-scale atmospheric pattern and its impact on the Transpolar Drift is provided. A more detailed description of the atmospheric conditions is given in Dethloff et al. (2021). Hereafter, we analyze the drift itself and reconstruct the course that the ship would have taken in previous years. This is followed by an analysis of ice concentration, ice thickness, snow thickness, and deformation and lead openings along the drift. Finally, we take a first glimpse at the distribution of melt ponds on the MOSAiC floe using high-resolution Sentinel-2 data collected before the CO entered Fram Strait and started to disintegrate. In closing, we summarize the main findings.

2 Material and Methods

The Transpolar Drift carried *Polarstern* with the MOSAiC CO from its initial position on October 4, 2019 (85°N, 136°E) to Fram Strait (July 31, 2020, 78.9°N, 2°E) within 303 days. Hereafter, the ship was relocated to a position near the North Pole (87.7°N, 104°E on August 21, 2020), an area with limited satellite coverage. In this manuscript we therefore exclusively focus on the first phase of the MOSAiC expedition.

The 303 days long drift is reconstructed using GPS data from different sensors: From October 4, 2019 to May 15, 2020, we use the ship's GPS. Because *Polarstern* had to leave the CO temporarily from mid of May until June 18 for the purpose of crew exchange, this period was bridged with GPS data provided by a surface buoy deployed on the CO prior departure (buoy ID P225, meereisportal.de, last access: December 29, 2020). For the remaining period until July 31, we again use ship GPS data. In the following, the data products utilised to describe the ice conditions in the vicinity of the MOSAiC floe are

https://doi.org/10.5194/tc-2021-80
Preprint. Discussion started: 8 April 2021
© Author(s) 2021. CC BY 4.0 License.


introduced. Where possible, we compare data in the full resolution of the respective satellite with mean values formed over a 50 and 100 km radius (Fig. 1, buffer).

2.1 Lagrangian sea-ice tracking

To investigate whether the 2019/2020 drift was comparable to previous years, we made use of satellite sea-ice motion data to reconstruct the pathways the ship would have taken if the experiment had started in one of the previous 14 years (October 2005 – 2018) instead. The satellite-based sea-ice pathways were determined with a drift analysis system called IceTrack. The system traces sea-ice forward in time using a combination of satellite-derived, low-resolution drift products (Krumpen et al., 2019 and 2020, Belter et al., 2020). In summary, IceTrack uses a combination of three different ice drift products for the tracking of sea-ice: i) motion estimates based on a combination of scatterometer and radiometer data provided by the Center for Satellite Exploitation and Research (CERSAT, Girard-Ardhuin and Ezraty, 2012, 62.5 x 62.5 km grid spacing), ii) the OSI-405-c motion product from the Ocean and Sea Ice Satellite Application Facility (OSISAF, Lavergne, 2016, 62.5 x 62.5 km grid spacing), and iii) Polar Pathfinder Daily Motion Vectors (v.4) from the National Snow and Ice Data Center (NSIDC, Tschudi et al., 2016, 25 x 25 km grid spacing). The IceTrack algorithm first checks for the availability of CERSAT motion data, since CERSAT provides the most consistent time series of motion vectors starting from 1991 to present and has shown good performance (Rozman et al., 2011; Krumpen et al., 2013). During summer months (June–July) when drift estimates from CERSAT are missing, motion information is bridged with the OSISAF product (2012 to present). Prior 2012, or if no valid OSISAF motion vector is available within the search range, NSIDC data are applied. The reconstruction of "virtual" floes for these 14 years works as follows: Sea-ice is traced forward in time on a daily basis starting on October 4 (1996 – 2019) until July 31 (303 days). Tracking is discontinued if ice concentration at a specific location along the trajectory drops below 50%, which the algorithm defines as the position where the ice melted.

To assess the accuracy of this Lagrangian tracking approach, Krumpen et al. (2019) reconstructed the pathways of 56 GPS buoys deployed between 2011 and 2016 in the central Arctic Ocean. The displacement between real and virtual tracks is approximately 36 ± 20 km after 200 days and considered to be in an acceptable range. To number the accuracy of IceTrack in 2019/2020, we reconstruct the drift of the CO and 23 additional DN buoys (Krumpen and Sokolov, 2020). A comparison of Fig. 2a with 2b (Supplement) shows that the reconstructed drift of the CO is in close agreement with the observed drift. However, when the CO entered Fram Strait (red box), the reconstructed track lags behind the real one. The limited performance of IceTrack in Fram Strait is the result of a general underestimation of drift speeds by low resolution satellite products in this area (Sumata et al., 2014). It becomes particularly evident when looking at the reconstructed drift of the additional 23 DN buoys deployed in the vicinity of the CO (Supplement S.1c). Within the first 200 days, the reconstructed DN trajectories deviate only slightly from real tracks (28 ± 15 km after 200 days), but once the DN reaches Fram Strait (south of 82.5°N, after 250 days), the distance between real and reconstructed pathways is gradually increasing. The comparison of the CO drift with the drift of the previous 14 years is therefore limited to the first 250 days.

2.2 Sea-ice concentration

A time series of sea-ice concentration along the MOSAiC trajectory between October to July (daily resolution) is obtained from the 89 GHz channels of the AMSR-E and AMSR2 microwave radiometer on the NASA Aqua and Jaxa GCOM-W satellites, respectively (Spreen et al., 2008; Melsheimer & Spreen, 2019a,b). Data is available from meereisportal.de and seaice.uni-bremen.de (last access: February 15, 2021). The spatial resolution of the data set is 6.25 km. The conditions in larger surroundings are determined by averaging all grid points falling within a 50 and 100 km radius (16 x 16 grid cells and 32 x 32 grid cells respectively). For comparison with previous years, we extracted sea-ice concentration along the MOSAiC trajectory for the years 2005/2006 to 2019/2020. The year 2011/2012 is left out due to a gap between AMSR-E and AMSR2. Uncertainties are below 5% for individual grid cells in winter and in the high ice concentration regime. In summer and at low

https://doi.org/10.5194/tc-2021-80
Preprint. Discussion started: 8 April 2021
© Author(s) 2021. CC BY 4.0 License.


ice concentration uncertainties can be significantly larger (up to 25%; Spreen et al., 2008). However, these are uncertainties of individual grid cells and mean biases for the averaged 50 and 100 km radii are lower. In summer or during warm air intrusions sea-ice underestimation due to wettened ice surfaces, ice lenses or higher liquid water content in the snow, or melt ponds might occur. Such a period is observed during MOSAiC from mid-April to May 2020 and discussed below. During that time period, we show for comparison sea-ice concentration from an inverse multi-parameter retrieval using optimal estimation (Scarlat et al., 2020). The spatial resolution of this dataset is approximately 40 km. During and following the warm air intrusion and associated rain on snow it shows more correct ice concentrations but is yet not available for the previous years and thus cannot be used as primary dataset here.

2.3 Sea-ice thickness

Sea-ice thickness (SIT) along the MOSAiC drift track during the Arctic winter season from October 2019 through April 2020 is analysed using two satellite remote sensing data sets. The first data set is based on radar altimeter data from the CryoSat-2 (CS2) mission of the European Space Agency (ESA). We use SIT retrievals generated at the full resolution of the altimeter with an approximate point spacing of 300 m and swath width of 1650 m along the ground-track of the satellite. The method of the SIT retrieval for each radar waveform is based on Ricker et al. (2014) with updates described in Hendricks et al. (2020). The data set is named the AWI CryoSat-2 sea-ice thickness product version 2.3 and it is accessible through the website meereisportal.de (last access: February 15, 2021). In this study, we specifically use the Level-2 pre-processed (l2p) product, which contains a daily collection of all data points along an orbit with valid freeboard data between October 1, 2019 and April 30, 2020. Subsets of all orbits within a day are generated based on their distance to the noon (UTC) position of the CO. For each subset we compute the mean SIT, the interquartile (IQR) and interdecile (ICR) SIT range, as well as the number of data points in each daily subset. According to the study logic, the search radius for the SIT subsets is chosen as 50 and 100 km and we only use individual orbits that provide at least 50 data points. Hence, we do not show data from a smaller (e.g. 5 km) search radius, as very few orbits were close enough to the CO.

The second data set used for the SIT estimation is the merged CryoSat-2/SMOS (CS2SMOS, version 203) SIT product (Ricker et al., 2017). CS2SMOS provides gridded SIT data at a resolution of 25 km, which is significantly lower than the CS2 l2p data, however the underlying optimal interpolation provides gapless SIT information, also north of the CS2 orbit limit of 88°N. Each daily updated CS2SMOS SIT field is based on an observation period of 7 days and we use the centre of this period as the reference time to subset SIT data around the CO position at the selected radii. CS2SMOS data are based on CS2 l2p and Soil Moisture and Ocean Salinity (SMOS) SIT data. The SMOS retrieval provides thickness information of thin sea sea-ice, which complements the CS2 l2p data. The data merging uses a background field extending two weeks before and after the observation period, thus the temporal coverage is shorter than that of the CS2 l2p data and ranges from October 18, 2019 to April 12, 2020. In addition, the selection of SIT observations in the CS2SMOS data may vary from the CS2 l2p regional coverage as we use the grid cell centre positions within 50 km and 100 km radius around the CO to compute the daily mean CS2SMOS SIT value. Thus, the number of CS2SMOS SIT observations selected may depend on the position of the CO relative to local grid cell coordinates. However, we do not expect this to cause a selection bias due to the smoothness of the CS2SMOS SIT data and the size of the search area.

2.4 Snow depth

Low resolution snow depth along the MOSAiC trajectory is retrieved from the 7 and 19 GHz channels of the AMSR2 microwave radiometer following the method from Rostosky et al. (2018) and is available via https://seaice.uni-bremen.de/data/amsr2/SnowDepth/ (last access: February 15, 2021). Following Rostosky et al. (2020), uncertainties are based on Monte-Carlo simulations using varying input parameters for a snow and sea-ice (MEMLS, Tonboe et al., 2006) and

https://doi.org/10.5194/tc-2021-80
Preprint. Discussion started: 8 April 2021
© Author(s) 2021. CC BY 4.0 License.


atmosphere (PAMTRA, Mech et al. 2020) microwave emission model. Most sea-ice, snow, and atmosphere properties are not known to the satellite snow depth retrieval (only information about the ice type, multi-year or first-year, is provided). Thus, by varying these properties and evaluating the influence on the snow depth retrieval, an estimate of the uncertainty caused by their unknown state can be obtained. The grid size of the snow depth data is 25 km. Snow depth currently can only be retrieved for multi-year ice areas in March and April (see Rostosky et al., 2018). As the MOSAiC ice floe is in an area of predominantly second-year ice, which radiometrically is considered multi-year ice for the snow depth retrieval, also snow depth for MOSAiC is only available for March and April. Here we present snow depth data at 12.5 km radius around the CO in addition to a 50 km and 100 km average. A comparison with previous years is made with snow depth data extracted along the MOSAiC drift from 2005 until 2019.

2.5 Lead detection based on optical data

Sea-ice leads, i.e. lead frequencies and lead fractions along the MOSAiC drift track are derived from Moderate-Resolution Imaging Spectroradiometer (MODIS) thermal infrared data and the Collection 6 of MYD/MOD29 ice surface temperatures (Hall and Riggs, 2019). In order to detect whether a lead is present in a certain pixel we employ the local surface temperature anomaly, which is expected to exhibit significant positive deviations when a lead is present during winter (November to April). This general procedure is followed by the application of a fuzzy inference system that assigns individual retrieval uncertainties to each detected lead pixel. Using this approach, we obtain daily categorical lead maps with separate classes for clouds, sea-ice, leads, and artefacts, with the latter comprising detected leads with an uncertainty exceeding 30%. The full approach and the resulting products are described in Reiser et al. (2020). From this data set we use daily lead data for the months of November to April for the years of 2005/2006 to 2018/2019 (as the reference period) and for the winter of 2019/2020 (for MOSAiC). Below lead data at 10 km resolution is compared with mean values formed over a 50 and 100 km radius. Note that days with a cloud fraction above 50 % are excluded from the analysis.

2.6 Sea-ice deformation from high resolution radar images

In this study, we quantify sea-ice deformation based on sequential Synthetic Aperture Radar (SAR) scenes obtained by ESA's Sentinel-1A/B satellites along the drift track of the CO. Deformation is the consequence of divergence (opening), convergence (closing) and shear (sliding alongside) between ice floes. Regularly gridded sea-ice drift and deformation fields with a spatial resolution of 1.4 km are retrieved following the method described in von Albedyll et al. (2020). More details about the drift algorithm are provided in Thomas et al. (2008 and 2011), and Hollands and Dierking (2011). As input for the applied algorithm, we use HH-polarized scenes with a spatial resolution of 50 m. Images over the CO are taken during the entire MOSAiC drift, except for the period between January 14 and March 15, when the ship was outside the satellite coverage. The temporal resolution is typically one image per day (with few exceptions). Spatial derivates are calculated from the gridded velocity field and used to derive convergence, divergence and shear (see von Albedyll et al. (2020) for details). To quantify deformation in the vicinity of the CO, we average all grid cells located within a 5 km radius around the ship. To compare deformation in the vicinity of the ship with deformation over a larger area (50 km), averages are computed for 61 x 5 km circles arranged within a radius of 50 km around the ship (see illustration in Fig. 3). In this way we avoid biases due to scaling effects. Exceptionally strong deformation events are defined as events with a magnitude exceeding two standard deviations.

2.7 Characterization of melt pond coverage using optical Sentinel-2 data

To provide a first quantification of the spatial distribution and temporal development of large melt ponds on the MOSAiC floe, we downloaded all available Sentinel-2 (S2, ESA) satellite images (https://scihub.copernicus.eu/dhus/, last access: February 10, 2021) taken over the ship between end of May and July 31, 2020. Prior the of May, the sun elevation was not high enough for passive optical remote sensing. A total of eight completely or partially cloud-free scenes could be identified. For the

https://doi.org/10.5194/tc-2021-80
Preprint. Discussion started: 8 April 2021
© Author(s) 2021. CC BY 4.0 License.


detection of melt ponds, we selected five scenes that are temporally equally spaced, namely June 21, July 1, July 7, July 22, and July 27, 2020. Next, the MOSAiC floe was clipped, and a pond index was calculated by means of a normalized spectral index (e.g. Gignac et al., 2017, Watson et al., 2018) using S2 bands 4 (665 nm) and 8 (842 nm) as input. The pond index is used to differentiate between water and ice/snow. Note that only ponds larger than the spatial resolution of the S2 sensor (10 m) can be detected. We therefore assume that the actual pond cover is significantly underestimated, and that the method is only suitable for providing estimates of the timing and relative changes in pond coverage.

2.8 Reanalysis and ship data

Mean sea-level pressure, 2 m temperature, and 10 m wind speed data for the time period 2005-2020 are derived from the newest version of the European Centre for Medium-range Weather Forecasts (ECMWF) global reanalysis, ERA5 (Hersbach et al. 2020). Hourly values along the MOSAiC trajectory in 2019/20 as well as in the preceding 14 years along the same trajectory are extracted by linear interpolation in time and space after triangulation of the rectangular ERA5-grid. The 2019/20 trajectory data are evaluated against corresponding standard meteorological observations on board of *Polarstern* (https://www.awi.de/nc/en/science/long-term-observations/atmosphere/polarstern.html, last access: February 22, 2021).

3 Results and Discussion

3.1 Atmospheric conditions and the Transpolar Drift in 2019/2020

Large-scale surface pressure and associated anomalies in 10 m wind speed (shown in Fig. 4) determined the course of the MOSAiC drift and its deviation from the long-term average. October, November, and December were characterized by moderate monthly mean circulation anomalies, oriented mostly such that the winds (and thus the drift) were westward rather than northward, thereby "deflecting" the MOSAiC drift from the North Pole. Starting in January, large-scale low-pressure entered the Arctic from the European sector, resulting in an intensification of the Transpolar Drift in January, February, and March (Fig. 5), with the low-pressure region gradually moving towards the Beaufort Sea. Correspondingly, these months were associated with an exceptionally high positive Arctic Oscillation (AO) index (see Dethloff et al. 2021 for a more detailed description). In April, the decaying low-pressure centre was located over the Beaufort Sea, resulting in a drift of the MOSAiC floe towards the Barents Sea. Next, the reversed pressure gradient in May, with a high-pressure anomaly over the Beaufort Sea, pushed the MOSAiC floe towards northeast Greenland until it entered the Fram Strait area (June/July).

Figure 6 compares ERA5-based atmospheric conditions along the MOSAiC drift trajectory with conditions in the preceding 14 years. The circulation anomalies from January through May (Fig. 4) led to positive temperature anomalies in northern Siberia and in the Kara and Laptev Seas, in particular in February (up to +10°C, not shown). In contrast, temperature anomalies at the MOSAiC floe were rather moderate most of the time (Fig. 6 middle). Moderate warmer-than-average periods occurred in mid-November, late February, mid-April, and late May, whereas colder-than-average periods occurred in early November and early March, with record-cold temperatures around -35°C. Wintertime cold (warm) anomalies were typically associated with high (low) surface pressure anomalies (Fig. 6 bottom). The positive AO months January, February, March, and April were accompanied by low pressure anomalies also at the MOSAiC floe (Fig. 6 bottom). Stormy conditions were encountered in particular in these months but also in late November/early December (Fig. 6 top). Apart from these exceptions, meteorological conditions at the MOSAiC floe can be considered relatively normal compared to previous years.

The ERA5 data along the MOSAiC trajectory in 2019/2020 agree well with co-located ship observations (Fig. 7), in particular regarding surface pressure. Wind speed tends to be slightly underestimated in ERA5, although it should be noted that the comparison with the raw on-board observations has limitations. However, the winter warm bias in ERA5 over Arctic sea ice of the order of 2-3°C (Fig.7) is consistent with previous assessments (e.g., Batrak and Müller 2019), especially taking into account that the ship temperatures are measured at 29 m with typically higher temperatures than the 2 m ERA5 reference

https://doi.org/10.5194/tc-2021-80
Preprint. Discussion started: 8 April 2021
© Author(s) 2021. CC BY 4.0 License.


temperature. Given that these differences are likely systematic and thus similar in other years, the anomalies discussed above are likely not strongly affected.

3.2 The MOSAiC drift and a comparison to previous years

We compared the drift of the MOSAiC floe with the course the CO would have taken if the experiment had started in any of the previous 14 years (October 2005 – 2018). The underlying satellite-based Lagrangian tracking approach is introduced in Section 2.1. Figure 8 summarizes the results of this analysis. Panel a) shows the reproduced MOSAiC trajectory (multi-colored line) together with trajectories from previous years (grey lines). The large differences between the tracks show how difficult it is to accurately predict the course of a drifting platform and how large the spread of possible endpoints can be. Panel b) provides the averaged satellite-derived daily displacement rates of the MOSAiC CO during the first 250 days as compared to the previous 14 years. With 8.52 km/d the drift speed in 2019/2020 is around 25% higher than the mean over the period from 2005 to 2018 (7.14 km/d ± 0.75). Only 2008/2009 shows an even higher average displacement rate (8.79 km/d), although Fram Strait is reached a few days later due to a more northerly route. Another striking year is 2018/2019, with only average daily displacement rates, but a strong westerly drift component which would have carried the ship even faster toward Fram Strait as in 2019/2020. The interannual variability seen in the mean displacement rates is mainly the result of differing large-scale atmospheric circulation regimes discussed in Section 3.1. A trend towards a faster Transpolar Drift as reported by Spreen et al. 2011 or Krumpen et al. 2019 cannot be deduced from this rather simple and spatially limited analysis. However, results shown here are in line with these studies.

3.3 Sea-ice concentration

Sea-ice concentration along the MOSAiC drift trajectory in 2019/2020 and the reference period 2005/2006 to 2018/2019 is shown in Figure 9. The average ice concentration between October 4, 2019 to July 31, 2020 amounts to 97%. The seasonal evolution is characterized by a substantial temporal variability over the course of the 303-day long drift. This variability is almost independent of the spatial scale used with only minor differences (±0.5 % deviation from mean) between the ice concentration values determined from the 3, 50, and 100 km radius (Fig. 10).

Given the high agreement between the different radii, will limit ourselves in the following to the discussion of the time series with the highest resolution (3 km radius, Fig. 9). From October to July the ice concentration along the MOSAiC drift trajectory agrees well with the long-term 2005/2006 to 2019/2020 average. However, during the first half of the drift (October until end of February) the ice concentration was with 99.5% about 1% higher than the long-term average, while during the second half (March until end of July), it was lower than the long-term average and shows higher variability than the first half.

Sea-ice concentration variability stayed below 5% until March 2020, when first significant reductions in ice concentration occurred. At this time, the CO was already positioned north of Fram Strait and the distance to the ice edge was gradually decreasing (compare Fig. 11). With the onset of spring in March/April first major drops in ice concentration below 90% occurred. The strong ice concentration reduction down to 75% from mid-April until beginning of May are due to a false satellite ice concentration retrieval. Observations from the ship confirm that the ice concentration stayed higher during that time period. We can see that at that time a warm air intrusion raised temperatures close to 0°C, which was accompanied by a significant increase in wind speed (Fig. 6). Already below 0°C liquid water content in the snow increases and later refreeze after the warming event can cause ice lenses in the snow. On the floe also refreezing rain on snow was observed. These surface processes and additional weather influence by high water vapour and cloud liquid water affect the microwave polarization difference and likely caused the unnatural fluctuation in ice concentration for the ASI algorithm used here. Other ice concentration algorithms for AMSR2 satellite data (e.g. NASA-Team) showed similar effects (not shown). As an alternative we present the ice concentration from an optimal estimation retrieval (Scarlat et al., 2020) during that critical time period in Figure 9, which takes such effects into account and is in better agreement with ship observations. After mid-May the ice

https://doi.org/10.5194/tc-2021-80
Preprint. Discussion started: 8 April 2021
© Author(s) 2021. CC BY 4.0 License.


concentration recovers to almost 100%. In July, the floe started to disintegrate and ice concentration dropped to 85% within a radius of 3 km around *Polarstern*, and below 60% in the 50 and 100 km radii (Fig. 10).

We determine the closest distance to the ice edge from sea-ice concentration maps (Fig. 11). At the beginning of the MOSAiC expedition, the distance from the CO to the ice edge was about 320 km. During October the distance gradually increased to 1000 km due to the freeze-up of the Russian marginal seas. Once the MOSAiC CO approached Fram Strait (March 2020) the distance to the ice edge steadily decreased until the ice margin was reached at the end of July 2020. Note that the winter variability in ice edge distance is caused by polynya activity on the Russian shelf seas.

3.4 Sea-ice thickness

Both satellite-based sea-ice thickness products show the expected increase in ice thickness between October 2019 and April 2020 (Fig. 12 and Table 1). Except for the period between February 14 to March 8, when the CO was positioned north of 88°N, the high orbit density of CS2 allows almost continuous daily coverage at 50 and 100 km radius. The monthly mean thickness within a 50 km (100 km) radius around the CO changed from 0.77 m (0.8 m) in October 2019 to 2.40 m (2.51 m) in April, 2020. The sea-ice thickness distribution is characterized with the interquartile range (IQR) as difference between 75% and 25% percentile and the interdecile range (IDR) as difference between 90% and 10% percentile. The increase in sea-ice thickness was accompanied by a similarly increased IQR and IDR, indicating a wider sea-ice thickness distribution as a result of thermodynamic ice growth and deformation of the older ice class and the formation of young ice throughout the winter season. It is notable that the CS2 L2P sea-ice thickness was consistently thinner at the 50 km radius compared to the 100 km radius (Tab. 1, on average 6 cm (4 %) between October and April). Similarly, IQR and IDR were larger for 100 km than for 50 km, however the larger number of data points in the wider search area may also lead to a higher likelihood of diverse sea-ice conditions. This is in agreement with findings of Krumpen et al. (2020). According to the authors, the MOSAiC DN was set up at a regional thickness minimum. The local minimum is related to the ice age: Sea ice in the DN was formed three weeks later than the surrounding ice. However, the authors report even larger differences in sea-ice thickness of 36% between the DN area and areas further away.

Results from CS2SMOS mirror these findings of thinner ice close to the CO compared to the larger scale, though the difference are smaller (Fig. 12, Table 1). This can be expected, as the primary input to the CS2SMOS analysis in the central Arctic is CS2 data due to its higher sensitivity to thicker ice than SMOS. The main differences to CS2 L2P are therefore the influence of SMOS in the beginning of the winter and the larger degree of smoothing introduced by the optimal interpolation. The monthly mean sea-ice thickness values in Table 1 are therefore mainly consistent with the exception of the October and November 2019. In this period, CS2SMOS was consistently higher by approximately 0.15m with respect to the CS2 L2P data. We do not expect that the locally lower thicknesses in the DN are well represented in the CS2SMOS thicknesses, since these are influenced by a larger region due to the interpolation method. The CS2 L2P thicknesses instead are effectively point measurements at kilometre scale and are apparently able to pick up the local thickness gradient. The discrepancy between the CS2 L2P and CS2SMOS thicknesses persisted well into November 2019 and became less prominent afterwards. This provides evidence that the local thickness minimum at the MOSAiC DN became less prominent over the winter season, though still at a detectable level as indicated by the consistently but minor differences at radii of 50 and 100 km.

Since CS2 L2P and CS2SMOS are in general consistent over the winter season, we use CS2SMOS data to compare sea-ice conditions during the MOSAiC drift with the past nine winter seasons in the CS2SMOS data record (Fig. 13). The comparison between the years shows a comparably low sea-ice thickness in the 10-year long data record at the location of the MOSAiC experiment, if not the lowest for segments in the earlier part of the drift. The monthly sea-ice thickness during MOSAiC was approximately 0.4 m lower at the beginning of the drift compared to mean monthly CS2SMOS of all previous winters (Table 1). The differences reduced towards 0.3 m in April, indicating slightly stronger thermodynamic and dynamic ice growth with respect to the average, potentially aided by the thinner sea-ice in the beginning. Again, the sea-ice thickness difference is

https://doi.org/10.5194/tc-2021-80
Preprint. Discussion started: 8 April 2021
© Author(s) 2021. CC BY 4.0 License.


stronger for the 50 km radius than the 100 km radius indicating that the MOSAiC experiment took place in a local sea-ice thickness minimum.

3.5 Snow depth

Figure 14 shows a time series of satellite-based snow thickness in March/April for the years between 2005 and 2020. The mean March-April snow depth during the MOSAiC year was 22 cm at the 12.5 km radius (22/23 cm in 50/100 km radius) with an uncertainty of 5 cm. Note that the observed snow thickness during MOSAiC is around 3 cm lower than the long-term average of years 2005 to 2019. A preliminary comparison (not shown) of satellite-based snow thickness estimates with in-situ observations from the MOSAiC CO indicates a good agreement with errors not exceeding the expected uncertainties.

The snow depth during MOSAiC was a few centimetres lower but overall, quite average from a satellite microwave radiometer perspective. The time series in Figure 14 shows that the snow depth stayed almost constant from beginning of March until mid-April. Only after the warm air intrusion in April (Fig. 6), increased precipitation led to a small increase in snow depth of about 3 cm. After the initial temperature increase snow depth reduced again, i.e., snow compacted. Mind that the microwave radiometer satellite snow depth retrieval does not react immediately to new snow, which has low emissivity and little scattering. The added snow usually shows up after the first few days of snow compaction, which is in line with the in-situ observation from the floe, where snow depth only increased after April 20 while the air temperatures already increased about five days earlier.

3.6 Leads

Lead frequencies and lead fractions are derived for the surroundings of the MOSAiC CO and the reference period using the method described in Reiser et al. (2020). The lead frequency is a temporally integrated quantity indicating how often a lead is found at a certain position within a defined period. The mean winter lead frequency (November to April between 2005/2006 and 2018/2019) for the central Arctic Basin and adjacent seas is shown in Figure 15a. The climatology shows that between November and April the central Arctic Ocean is generally characterised by low lead frequencies with values of roughly 0.1. This agrees well with consistently high ice concentration values indicated by the sea-ice concentration climatology during the first half of the expedition (Fig. 9). According to the climatology, higher lead frequencies (> 0.15) in winter are only to be expected near the ice edge and in Fram Strait. The lead frequency anomalies for the MOSAiC year 2019/2020 shown in Fig. 15b indicate no significant deviations from the winter mean climatology. On average, anomalies were slightly negative along the MOSAiC drift trajectory and in the sector between 30°W and 120°E, which again agrees well with the observed slightly higher ice concentration values as compared to the long-term mean (Fig. 9).

Regional differences in lead frequencies can be inferred from monthly lead anomaly maps shown in Fig. 15c-h: The monthly maps reveal anomalously high lead frequencies north of Greenland and Ellesmere Island between November and January. Moreover, the strong positive anomalies in the Barents Sea in January and in the Beaufort Sea in February/March are worth mentioning (compare Dethloff et al. 2021). However, in the proximity of the CO no significant lead anomalies are found between November and February. Only in March, when the CO was crossing a region of East-West oriented leads, slightly higher anomaly values of up to 0.1 are indicated. In April, leads around the MOSAiC CO were more North-South oriented and strengthened as expressed by higher anomaly values of up to 0.2 (Fig. 15h).

A detailed view on the temporal evolution of lead fractions along the MOSAiC drift trajectory on different radii is presented in Figure 16. Lead fraction is shown for the area around the MOSAiC CO with 10 km, 50 km and 100 km radius, respectively, together with the mean and maximum lead fraction for the reference period and one standard deviation. The mean lead fraction for the area around the CO was slightly increasing towards the end of winter for all of the three ranges shown, which confirms the drift into a region with generally higher average lead frequencies starting in March (Fig. 16a). In general, lead dynamics around the MOSAiC CO were typical for the respective region and point in time with only a few temporally limited, but

https://doi.org/10.5194/tc-2021-80
Preprint. Discussion started: 8 April 2021
© Author(s) 2021. CC BY 4.0 License.


significant deviations from the mean. However, meaningful conclusions can only be drawn for the periods in which the cloud fraction for the respective radii was below 50%. Note that in Figure 16 days with missing data and higher cloud fractions are indicated by red dots. A maximum in lead activity was observed on March 4 (at all radii). Several smaller events with lead fractions exceeding one standard deviation from the reference period were recorded on December 11 – 12, January 19, January 28, February 1, February 4 – 8, March 1 – 5, March 11, and April 23 - 24 (for 50 km radius, Fig. 16a.). It is striking that these events were only conditionally accompanied by a decrease in ice concentration.

3.7 Sea-ice deformation

Figure 17 shows the time series of divergence and shear rates along the MOSAiC drift track at 5 km and 50 km radii as obtained from Sentinel-1 SAR data. Overall, we find that deformation close to the ship (5 km radius), was representative for the deformation acting on the ice cover at larger distances (up to 50 km). Moreover, we find that mean shear and divergence of 8 % d^{-1} and 2 % d^{-1} along the MOSAiC drift track are in good agreement with deformation rates obtained from a ship-radar North of Svalbard by Oikkonen et al. (2017).

The variability of divergence and shear showed a seasonal behavior which is linked to the consolidation of the ice pack and in agreement with findings of previous studies (e.g., Itkin et al., 2017, Hutchings et al., 2011.). Monthly averages of the time series indicates that deformation was moderate and balanced in convergence and divergence in the consolidation phase between October and November (Fig. 17). Hereafter, divergence and shear temporarily decreased from December to January. In March to May, divergence and shear went back to a moderate level until a sudden increase in June and July was observed when the MOSAiC CO approached the marginal ice zone. Note that monthly averaged divergence correlates reasonably well with intensified lead activity observed by optical satellites (Sect. 3.6). In spring (March, April), the ice experienced more divergent than convergent motion, which again agrees well with intensified lead activity observed in spring (Fig. 15/16).

On daily time scales, divergence and shear were characterized by long quiet phases occasionally interrupted by strong deformation events (video supplement). The average temporal spacing between such deformation events was 2.5 weeks. However, the events were not uniformly distributed in time, as 60 % of the events took place between October and November (grey bars in Fig. 17). The strongest deformation event within the 50 km radius of the CO was observed on April 14-17, 2020. By that time, a lead of almost 2.5 km width opened up at 25 km distance of the CO (Fig. 3).

3.8 Melt pond distribution

Figure 18 presents five cloud-free S2 scenes obtained between June 21 and July 27 that provide a first overview of the temporal and spatial evolution of melt ponds on the MOSAiC floe and its extended surroundings. Melt pond coverage is characterized using the pond index described in Section 2.7, where high values indicate water and low values ice/snow.

One of the most striking features is that at the time when the first cloud-free scene (July 21) was taken, large melt ponds had already developed on the MOSAiC floe. The earlier start of melt pond formation on the MOSAiC floe as compared to the extended surrounding is likely related to the surface topography. Compared to the surrounding floes, the MOSAiC floe was characterized by heavily deformed areas which may have favoured early accumulation of large meltwater ponds. Another possible reason for the early onset of melting may be the high quantity of sediments that were trapped in the ice (Krumpen et al. 2020). The high sediment content temporarily reduced the surface albedo of the floe, which may have favoured early melt of ice.

Within the next ten days, the proportion of large melt ponds on the MOSAiC floe increased considerably, and large ponds also began to form on the neighbouring floes. On July 7, while the total amount of melt ponds was still increasing, a few large melt ponds began to drain. In the final scene (July 27), taken almost three weeks after the draining began and just before the floe was abandoned, large melt ponds had mostly split into smaller ponds and had partially disappeared as a result of several drainage events that were observed in field between July 1 and 27. The (absolute) quantification of melt pond fraction is

https://doi.org/10.5194/tc-2021-80
Preprint. Discussion started: 8 April 2021
© Author(s) 2021. CC BY 4.0 License.


limited, as the typical size of the melt ponds observed on the ground were equal to or smaller than the pixel size of the S2 image.

4 Conclusion

Below we summarize the ice conditions along the drift of the MOSAiC floe and the extended surroundings and compare them to previous years. The analysis is based on satellite data products commonly used for the scientific analysis of sea-ice in the Arctic Ocean. An overview of the atmospheric and sea-ice conditions observed along track is given in Fig. 19.

- A comparison of the MOSAiC trajectory with reconstructed satellite-based pathways for the past 14 years indicates that the drift during the first 250 days of the expedition was around 25% faster than the climatological mean drift. Deviations from a long-term average drift path are to a large extent the consequence of prevailing large-scale low-pressure anomalies, which resulted in an intensification of the Transpolar Drift between January and March 2020.
- CS2 and CS2SMOS data records show that the mean thickness of sea-ice around the CO (50 km radius) evolved from 0.77 m in October 2019 to 2.40 m in April 2020. Sea-ice near the CO (50 km radius) was thereby 4% thinner as compared to surrounding sea-ice (100 km radius). According to Krumpen et al. (2020), the negative anomaly is due to the younger ice age, as the ice around the CO was formed in a different region and later in the year than the surrounding ice. A comparison with CS2SMOS records from the past nine winters shows that the ice around the MOSAiC CO was comparatively thin (partially the thinnest). In October it was 0.4 m and in April 0.3 m below the nine year average.
- Unlike the ice thickness, the snow thickness does not differ much from the long-term mean. Data from satellite-based microwave radiometers indicate an average March/April snow depth of 22 cm (25 km radius). This is 3 cm lower than the long-term mean for the years 2006 to 2019.
- From the start of the expedition until April, the average ice concentration within the 50 km radius of the CO was slightly higher (1%) than the long-term mean with low variability. Significant changes in the ice cover occurred only in April and May, as a result of a positive temperature anomaly. Another significant drop in ice concentration took place at the end of the first expedition phase when the floe approached the ice edge (July).
- An analysis of winter (October – April) lead frequencies inferred from MODIS thermal infrared data indicates no significant deviation in lead activity from the mean climatology (2005/2006 – 2018/2019). At most, a slight negative deviation from the winter mean is discernible, which agrees well with the positive anomaly in ice concentration between October and April. It is interesting to note that with increasing variability in ice concentration from March onwards, lead activity increased.
- A deformation time series derived from Sentinel-1 data gives first insights into divergence and shear events along the MOSAiC drift. Overall, we find that sea-ice deformation on the 5 km radius including the MOSAiC CO was representative for the wider (50 km radius) surroundings. Deformation rates were lower during winter, and higher during summer, which is in agreement with observations from previous studies. The dominance of divergence during spring and summer agrees well with the observed higher lead fractions.
- Five cloud-free S2 scenes obtained during the melting phase provide insight into temporal and spatial evolution of melt pond coverage on the MOSAiC floe. Particularly worth mentioning is that formation of melt ponds began earlier on the MOSAiC floe than on neighbouring floes.

Acknowledgement

This work was supported by the German Ministry for Education and Research (BMBF) as part of the Russian-German Research Cooperation WTZ-RUS QUARCCS (grant 03F0777A) and CATS (grant 03F0831C), the International Multidisciplinary drifting Observatory for the Study of the Arctic Climate (grant MOSAiC20192020, AWI_PS122_00),

© Author(s) 2021. CC BY 4.0 License.

IceSense (grants 03F0866B and 03F0866A), and the Seamless Sea Ice Prediction project (SSIP; grant 01LN1701A). We acknowledge support by the Deutsche Forschungsgemeinschaft (DFG) project 268020496–TRR 172, within the Transregional Collaborative Research Center "Arctic Amplification: Climate Relevant Atmospheric and Surface Processes, and Feedback Mechanisms (AC)^3. ERA5 data were generated and provided by ECMWF and the Copernicus Climate Change Service. The work on satellite remote sensing data was partly funded through the EU H2020 project SPICES (640161), the ESA Sea Ice CCI phase 1 and 2 (AO/1-6772/11/I-AM) and the Helmholtz PACES II (Polar regions And Coasts in the changing Earth System) and FRAM (FRontiers in Arctic marine Monitoring) program. The production of the CryoSat-2/SMOS sea-ice thickness data was funded by the ESA project SMOS & CryoSat-2 Sea Ice Data Product Processing and Dissemination Service (ESA Contract No. 4000124731/lS/I-EF).

Code/data availability

All data is archived in the MOSAiC Central Storage (MCS) and will be available on PANGAEA after finalization of the respective datasets according to the MOSAiC data policy. The gridded CryoSat/SMOS data sets are available via ftp://ftp.awi.de/sea_ice/product/cryosat2_smos/v203/nh/ and documentation can be found at https://earth.esa.int/eogateway/catalog/smos-cryosat-l4-sea-ice-thickness. The sea-ice concentration and snow depth data are available at https://seaice.uni-bremen.de and until 2018 from PANGAEA (Melsheimer & Spreen, 2019a, 2019b). NCEP Reanalysis 2 data are made available by NOAA/OAR/ESRL PSD, Boulder, Colorado, USA, from their website at https://www.esrl.noaa.gov/psd/. This work contains modified Copernicus Sentinel data [2019/2020]. Sentinel-1 scenes are available from the Copernicus Open Access Hub (https://scihub.copernicus.eu/dhus/home).

Competing interests

The authors declare no competing interests.

Author contributions

T.K., L.v.A., H. G., S. H, B. J., G. S. & S. W. conceived the study and wrote the paper. J. B., C. H., L. K., C. K., X. T. K., R. R., J. R., S. S. & J. S. provided data, contributed to the analysis and discussion.

Video Supplement

Time series of shear and divergencefields along the drift track of the MOSAiC floe from October 5, 2019 to July 14 2020. Ice drift is displayed as arrows while deformation is shown as colors. The title states the time period for which the deformation was calculated. The white circle around the *Polarstern* position has a 5 and 50 km radius (https://doi.org/10.5446/51302)

References

Alfred Wegener Institute: Polar Research and Supply Vessel *Polarstern* Operated by the Alfred Wegener Institute Helmholtz Centre for Polar and Marine Research. Journal of large-scale research facilities, 3, A119, http://dx.doi.org/10.17815/jlsrf-3-163 , 2017.

Batrak, Y., Müller, M. On the warm bias in atmospheric reanalyses induced by the missing snow over Arctic sea-ice. Nat Commun 10, 4170. https://doi.org/10.1038/s41467-019-11975-3, 2019.

Dethloff, K., Maslowski, W., Hendricks, S., Lee, Y., Goessling, H. F., Krumpen, T., Haas, C., Handorf, D., Ricker, R., Bessonov, V., Cassano, J. J., Kinney, J. C., Osinski, R., Rex, M., Rinke, A., Sokolova, J., and Sommerfeld, A.: Arctic sea ice anomalies during the MOSAiC winter 2019/20, The Cryosphere Discuss., https://doi.org/10.5194/tc-2020-375, in review, 2021.

© Author(s) 2021. CC BY 4.0 License.

Ezraty, R., Girard-Ardhuin, F., Piolle, J. F., Kaleschke, L., Heygster, G.: Arctic and Antarctic Sea Ice Concentration and Arctic Sea Ice Drift Estimated from Special Sensor Microwave Data, Technical Report, Departement d'Oceanographie Physique et Spatiale, IFREMER, Brest, France, 2007.

Gignac, C., Bernier, M., Chokmani, K., & Poulin, J. (2017). IceMap250—Automatic 250 m sea ice extent mapping using MODIS data. Remote Sensing, 9(1), 70. https://doi.org/10.3390/rs9010070

Girard-Ardhuin, F., Ezraty, R.: Enhanced arctic sea-ice drift estimation merging radiometer and scatterometer data. IEEE Transaction in Geoscience and Remote Sensing Recent advances in C-band scatterometry Special Issue **50**(7), 2639–2648, 2012.

Hall, D.K., Riggs, G.: MODIS/Terra Sea Ice Extent 5-Min L2 Swath 1km, Version 6. [Northern Hemisphere]. Available online: https://nsidc.org/data/MOD29/versions/6 (accessed on 15 October 2019).

Hendricks, S. and Ricker, R.: Product User Guide and Algorithm Specification: AWI CryoSat-2 Sea Ice Thickness (version 2.3), https://epic.awi.de/id/eprint/53331/, 2020.

Hersbach, H, Bell, B, Berrisford, P, et al. The ERA5 global reanalysis. Q J R Meteorol Soc.; 146: 1999– 2049. https://doi.org/10.1002/qj.3803, 2020.

Hollands, T. and Dierking, W.: Performance of a multiscale correlation algorithm for the estimation of sea-ice drift from SAR images: initial results, Annals of Glaciology, 52, 311–317, https://doi.org/10.3189/172756411795931462, 2011.

Hutchings, J. K., A. Roberts, C. A. Geiger, and J. Richter-Menge, Spatial and temporal characterization of sea-ice deformation, Annals of Glaciology, 52 (57), 360{368, doi:10.3189/172756411795931769, 2011.

Itkin, P., Spreen, G., Hvidegaard, S. M., Skourup, H., Wilkinson, J., Gerland, S., and Granskog, M. A.: Contribution of Deformation to Sea Ice Mass Balance: A Case Study From an N-ICE2015 Storm, Geophysical Research Letters, 45, 789–796, https://doi.org/10.1002/2017gl076056, 2018.

Jakobsson, M., Mayer, L., Coakley, B, Dowdeswell, J., Forbes, S., Fridman, B., Hodnesdal, H., Noormets, R., Pedersen, R., Rebesco, M., Schenke, H. W., Zarayskaya, Y., Accettella, D., Armstrong, A., Anderson, R. M., Bienhoff, P., Camerlenghi, A., Church, I., Edwards, M., Gardner, J., Hall, J., Hell, B., Hestvik, O., Kristoffersen, Y., Marcussen, C., Mohammad, R., Mosher, D., Nghiem, S., Pedrosa, M., Travaglini, P., Weatherall, P.: The International Bathymetric Chart of the Arctic Ocean (IBCAO) Version 3.0, Geophysical Research Letters, 39, , L12609, https://doi.org/10.1029/2012GL052219, 2012.

Kanamitsu, M., Ebisuzaki, W., Woollen, J., Yang, S. K., Hnilo, J. J., Fiorinom M., Potter, G., H.: NCEP-DOE AMIP-II Reanalysis (R-2), Bulletin of the American Meteorological Society, 83, 1631-1643, 2002.

Krumpen, T., Janout, M., Hodges, K. I., Gerdes, R., Girard-Ardhuin, F., Hoelemann, J. A., Willmes, S.: Variability and trends in Laptev Sea-ice outflow between 1992 – 2011, The Cryosphere, 7, 349-363, https://doi.org/10.5194/tc-7-349-2013, 2013.

Krumpen, T. and Sokolov, V.: The Expedition AF122/1 : Setting up the MOSAiC Distributed Network in October 2019 with Research Vessel AKADEMIK FEDOROV, Berichte zur Polar- und Meeresforschung = Reports on polar and marine research, Bremerhaven, Alfred Wegener Institute for Polar and Marine Research, 744 , 119 pp., https://doi.org/10.2312/BzPM_0744_2020, 2020.

Krumpen, T., Belter, J., Boetius, A., Damm, E., Haas, C., Hendricks, S., Nicolaus, M., Nöthig, E. M. , Paul, S., Peeken, I., Ricker, R., and Stein, R.: Arctic warming interrupts the Transpolar Drift and affects longrange transport of sea-ice and ice-rafted matter, Sci. Rep., 9, 5459, https://doi.org/10.1038/s41598-019-41456-y, 2019.

Krumpen, T., Birrien, F., Kauker, F., Rackow, T., von Albedyll, L., Angelopoulos, M., Belter, H. J., Bessonov, V., Damm, E., Dethloff, K., Haapala, J., Haas, C., Harris, C., Hendricks, S., Hoelemann, J., Hoppmann, M., Kaleschke, L., Karcher, M., Kolabutin, N., Lei, R., Lenz, J., Morgenstern, A., Nicolaus, M., Nixdorf, U., Petrovsky, T., Rabe, B., Rabenstein, L., Rex, M., Ricker, R., Rohde, J., Shimanchuk, E., Singha, S., Smolyanitsky, V., Sokolov, V., Stanton, T., Timofeeva, A., Tsamados, M., and Watkins, D.: The MOSAiC ice floe: sediment-laden survivor from the Siberian shelf, The Cryosphere, 14, 2173–2187, https://doi.org/10.5194/tc-14-2173-2020, 2020.

© Author(s) 2021. CC BY 4.0 License.


Lavergne, T.: Validation and Monitoring of the OSI SAF Low Resolution Sea Ice Drift Product (v5). Technical Report, The EUMETSAT Network of Satellite Application Facilities, July, 2016.

Mech, M., Maahn, M., Kneifel, S., Ori, D., Orlandi, E., Kollias, P., Schemann, V., and Crewell, S.: PAMTRA 1.0: the Passive and Active Microwave radiative TRAnsfer tool for simulating radiometer and radar measurements of the cloudy atmosphere, Geosci. Model Dev., 13, 4229–4251, https://doi.org/10.5194/gmd-13-4229-2020, 2020.

Melsheimer, C. and G. Spreen: AMSR2 ASI sea-ice concentration data, Arctic, version 5.4, July 2012 – December 2018 Pangaea, Doi:10.1594/PANGAEA.898399, 2019a

Melsheimer, C. and G. Spreen: AMSR-E ASI sea-ice concentration data, Arctic, version 5.4, June 2002 - September 2011) Pangaea, doi:10.1594/PANGAEA.899090, 2019b

Oikkonen, A., J. Haapala, M. Lensu, J. Karvonen, and P. Itkin, Small-scale sea-ice deformation during n-ICE2015: From compact pack ice to marginal ice zone, Journal of Geophysical Research: Oceans, 122 (6), 5105{5120, doi: 10.1002/2016jc012387, 2017.

Reiser, F., Willmes, S. and Heinemann, G.: A New Algorithm for Daily Sea Ice Lead Identification in the Arctic and Antarctic Winter from Thermal-Infrared Satellite Imagery. Remote Sens., 12(12), 1957; https://doi.org/10.3390/rs12121957, 2020.

Ricker, R., Hendricks, S., Helm, V., Skourup, H., and Davidson, M.: Sensitivity of CryoSat-2 Arctic sea-ice freeboard and thickness on radar-waveform interpretation, The Cryosphere, 8, 1607–1622, https://doi.org/10.5194/tc-8-1607-2014, 2014.

Ricker, R., Hendricks, S., Kaleschke, L., Tian-Kunze, X., King, J., and Haas, C.: A weekly Arctic sea-ice thickness data record from merged CryoSat-2 and SMOS satellite data, The Cryosphere, 11, 1607-1623, https://doi.org/10.5194/tc-11-1607-2017, 2017.

Rostosky, P., G. Spreen, S. L. Farrell, T. Frost, G. Heygster, and C. Melsheimer: Snow Depth Retrieval on Arctic Sea Ice From Passive Microwave Radiometers-Improvements and Extensions to Multiyear Ice Using Lower Frequencies. J. Geophys. Res. Oceans, 123, 7120–7138, https://doi.org/10.1029/2018jc014028, 2018.

Rostosky, P., G. Spreen, S. Gerland, M. Huntemann, and M. Mech: Modeling the Microwave Emission of Snow on Arctic Sea Ice for Estimating the Uncertainty of Satellite Retrievals. J. Geophys. Res. Oceans, 125, https://doi.org/10.1029/2019jc015465, 2020.

Rozman, P., Hoelemann, J., Krumpen, T., Gerdes, R., Koeberle, C., Lavergne, T., and Adams, S.: Validating satellite derived and modelled sea-ice drift in the Laptev Sea with in situ measurements from the winter of 2007/08. Polar Research, 30(7218), 2011.

Scarlat, R. C., G. Spreen, G. Heygster, M. Huntemann, C. Patilea, L. Toudal Pedersen, and R. Saldo: Sea Ice and Atmospheric Parameter Retrieval From Satellite Microwave Radiometers: Synergy of AMSR2 and SMOS Compared with the CIMR Candidate Mission. J. Geophys. Res. Oceans, 125(3), e2019JC015749, 2020.

Spreen, G., L. Kaleschke, and G. Heygster: Sea-ice remote sensing using AMSR-E 89-GHz channels. J. Geophys. Res., 113, C02S03, https://doi.org/10.1029/2005JC003384, 2008.

Spreen, G., Kwok, R., and Menemenlis, D.: Trends in Arctic sea-ice drift and role of wind forcing: 1992-2019, Geophysical Research Letters, 38 (19), https://doi.org/10.1029/2011GL048970, 2011.

Sumata, H., Lavergne, T., Girard-Ardhuin, F., Kimura, N., Tschudi, M. A., Kauker, F., Karcher, M., and Gerdes, R.: An intercomparison of Arctic ice drift products to deduce uncertainty estimates, J. Geophys. Res.-Oceans, 119, 4887–4921, 2014.

Thomas, M., Geiger, C., and Kambhamettu, C.: High resolution (400 m) motion characterization of sea ice using ERS-1 SAR imagery, Cold Regions Science and Technology, 52, 207–223, https://doi.org/10.1016/j.coldregions.2007.06.006, 2008.

Thomas, M., Kambhamettu, C., and Geiger, C. A.: Motion Tracking of Discontinuous Sea Ice, IEEE Transactions on Geoscience and Remote Sensing, 49, 5064–5079, https://doi.org/10.1109/tgrs.2011.2158005, 2011.

https://doi.org/10.5194/tc-2021-80
Preprint. Discussion started: 8 April 2021
© Author(s) 2021. CC BY 4.0 License.

Tonboe, R. T., Heygster, G., Pedersen, L. T., & Andersen, S.; Sea ice emission modelling. In Mätzler, C. (Ed.), Thermal microwave radiation: Applications for remote sensing (Vol. 52, pp. 382–425). London, UK: IEE Electromagnetic Waves Series, 2006.

Tschudi, M., Fowler, C., Maslanik, J., Stewart, J. S.: Polar Pathfinder Daily 25 km EASE-Grid Sea Ice Motion Vectors, Version 3. Technical report, NASA National Snow and Ice Data Center Distributed Active Archive Center., Boulder, Colorado USA, 2016.

von Albedyll, L., Haas, C., and Dierking, W.: Linking sea ice deformation to ice thickness redistribution using high-resolution satellite and airborne observations, The Cryosphere Discuss. [preprint], https://doi.org/10.5194/tc-2020-303, in review, 2020.

Watson, C. S., King, O., Miles, E. S., & Quincey, D. J.: Optimising NDWI supraglacial pond classification on Himalayan debris-covered glaciers. Remote sensing of environment, 217, 414-425. https://doi.org/10.3390/rs9010070, 2018.

WMO: Sea Ice Nomenclature, WMO/OMM/BMO - No.259, Edition 1970 – 2017, Terminology, Volume I, 2017.

https://doi.org/10.5194/tc-2021-80
Preprint. Discussion started: 8 April 2021
© Author(s) 2021. CC BY 4.0 License.

Table 1: Monthly statistics of sea-ice thickness (SIT) from CryoSat-2 (CS2) level-2p (L2P) orbit and gridded CryoSat-2/SMOS (CS2SMOS) data for two radii around the CO position. The CS2 SIT distribution is characterized with the interquartile range (IQR) as difference between 75% and 25% percentile and the interdecile range (IDR) as difference between 90% and 10% percentile. For CS2SMOS, the SIT difference (ΔSIT) between the MOSAiC year and SIT from the same drift trajectory but of previous winters since 2010 is given. The asterisk (*) marks that the mean SIT of CS2SMOS depends on less years than the other month since the CS2SMOS data record only starts in November 2010.

	CS2 L2P						CS2SMOS			
	SIT (m)		SIT IQR (m)		SIT IDR (m)		SIT (m)		ΔSIT (m)	
	50 km	100 km	50 km	100 km	50 km	100 km	50 km	100 km	50 km	100 km
Oct 19*	0.77	0.80	0.47	0.51	0.93	1.04	0.95	0.97	-0.41	-0.38
Nov 19	1.02	1.07	0.52	0.60	1.05	1.23	1.13	1.15	-0.45	-0.43
Dec 19	1.26	1.31	0.57	0.62	1.14	1.27	1.35	1.37	-0.38	-0.35
Jan 20	1.46	1.48	0.61	0.63	1.21	1.28	1.50	1.51	-0.38	-0.36
Feb 20	1.90	1.99	0.69	0.79	1.39	1.60	1.99	2.00	-0.29	-0.28
Mar 20	2.23	2.27	0.85	0.88	1.74	1.81	2.31	2.33	-0.43	-0.41
Apr 20	2.40	2.51	1.21	1.24	2.33	2.40	2.50	2.51	-0.29	-0.27

https://doi.org/10.5194/tc-2021-80
Preprint. Discussion started: 8 April 2021
© Author(s) 2021. CC BY 4.0 License.

The Cryosphere
Discussions
Open Access
EGU

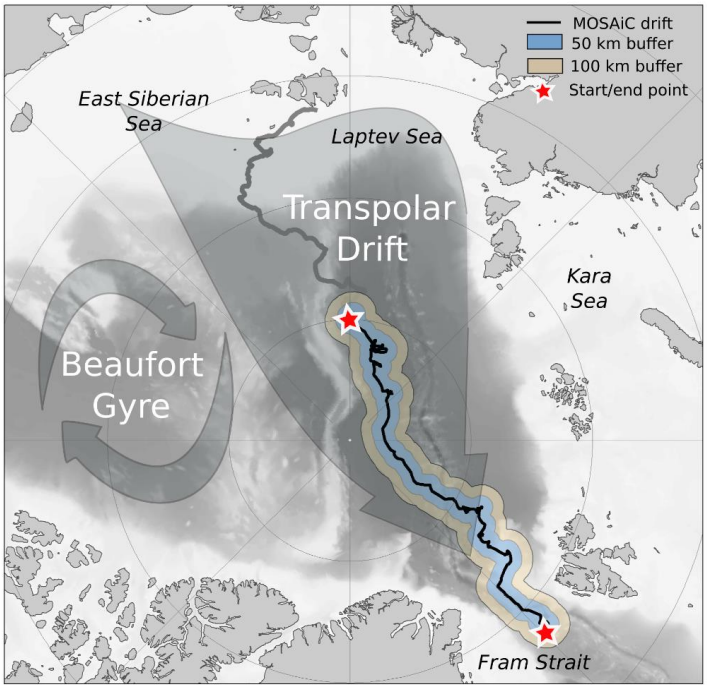

625

Figure 1: The MOSAiC drift (black line, the Central Observatory, CO) with a 50 km (blue) and 100 km (orange) buffer. Start (October 4, 2019) and end point (July 31, 2020) of the first MOSAiC expedition phase are indicated by red stars. Following Krumpen et al. (2020), the MOSAiC floe originated from the New Siberian Islands (grey thick line). The bathymetry of the Arctic Ocean (grey colors in the background) is based from Jakobsson et al. (2012)

630

https://doi.org/10.5194/tc-2021-80
Preprint. Discussion started: 8 April 2021
© Author(s) 2021. CC BY 4.0 License.

The Cryosphere Discussions
Open Access
EGU

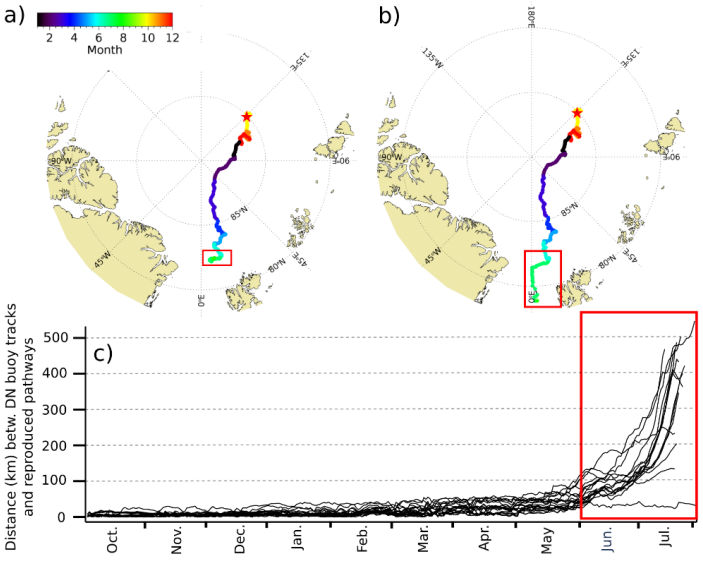

Figure 2: Comparison of MOSAiC CO and DN buoy tracks with IceTrack results: a) Reproduced pathway of the CO with IceTrack, b) Real (GPS-based) track of the CO, c) Distance between 23 DN buoys (source: seaiceportal.de) deployed on sea ice in the vicinity of the CO at the beginning of October 2019 and their reconstructed trajectories. Deviation between real and virtual tracks is small. Only once buoys enter Fram Strait (beginning of June (240 d) at 82.5°N), the displacement is gradually increasing.

https://doi.org/10.5194/tc-2021-80
Preprint. Discussion started: 8 April 2021
© Author(s) 2021. CC BY 4.0 License.

The Cryosphere Discussions
Open Access
EGU

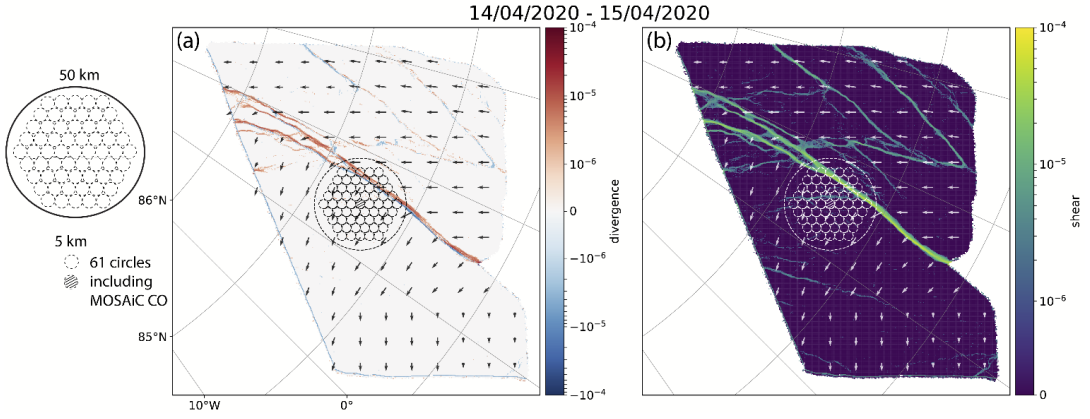

Figure 3: Left: To compare deformation in the vicinity of the ship (5 km) with deformation at larger distances (50 km), averages were computed for 61 x 5 km circles arranged within a radius of 50 km around the ship. Centre/right: Example of divergence (middle) and shear (right) derived from two consecutive Sentinel-1 SAR images acquired on April 14 (07:26:14) and 15 (08:07:03) 2020. Sea ice motion is displayed as black arrows. The image pair shows the strongest deformation event observed: Within 24 hours, a 2.5 km wide north-south oriented lead opened up ~25 km away from the CO.

https://doi.org/10.5194/tc-2021-80
Preprint. Discussion started: 8 April 2021
© Author(s) 2021. CC BY 4.0 License.

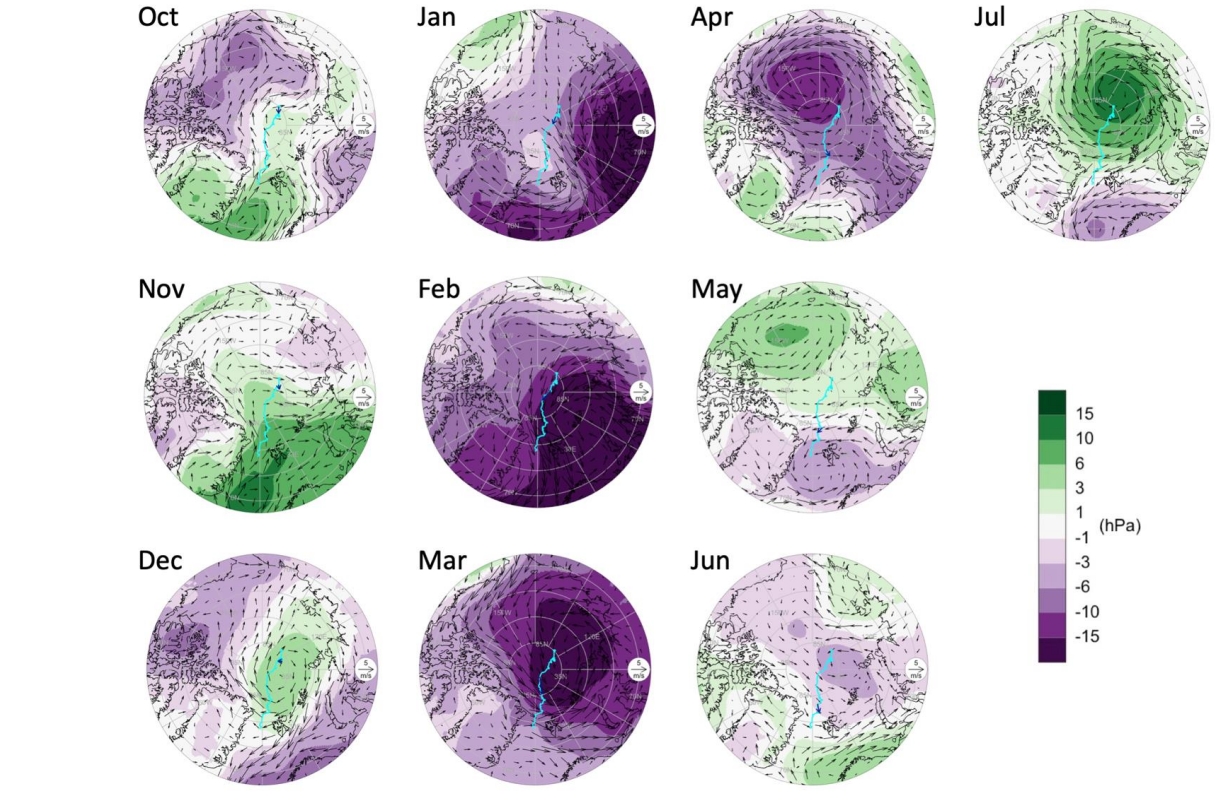

Figure 4: Monthly-mean sea-level pressure (shading) and 10m wind (arrows) anomalies with respect to the reference period 2005-2019 for each month of the MOSAiC drift from October 2019 to July 2020. The complete drift path is denoted by cyan lines; the drift during the respective month is denoted by blue arrows.

https://doi.org/10.5194/tc-2021-80
Preprint. Discussion started: 8 April 2021
© Author(s) 2021. CC BY 4.0 License.

The Cryosphere
Discussions
Open Access
EGU

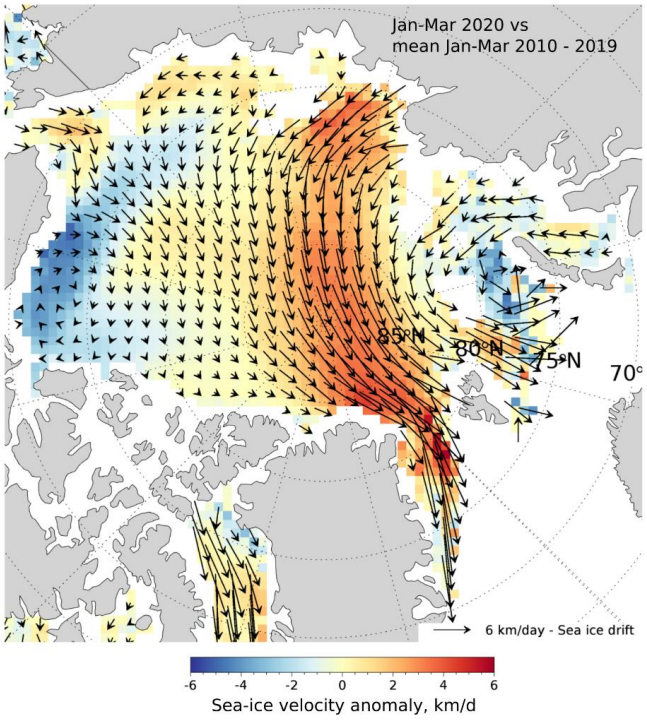

655

Figure 5: Three-month (January – March) sea-ice velocity anomalies in 2020 with respect to the reference period 2010-2019. Anomalies were computed from the OSI-405-c motion product provided by the Ocean and Sea Ice Satellite Application Facility (OSISAF, Lavergne, 2016). The vectors plotted on top indicate the average daily sea-ice motion for the same period (reprint from Dethloff et al. 2021).

660

https://doi.org/10.5194/tc-2021-80
Preprint. Discussion started: 8 April 2021
© Author(s) 2021. CC BY 4.0 License.

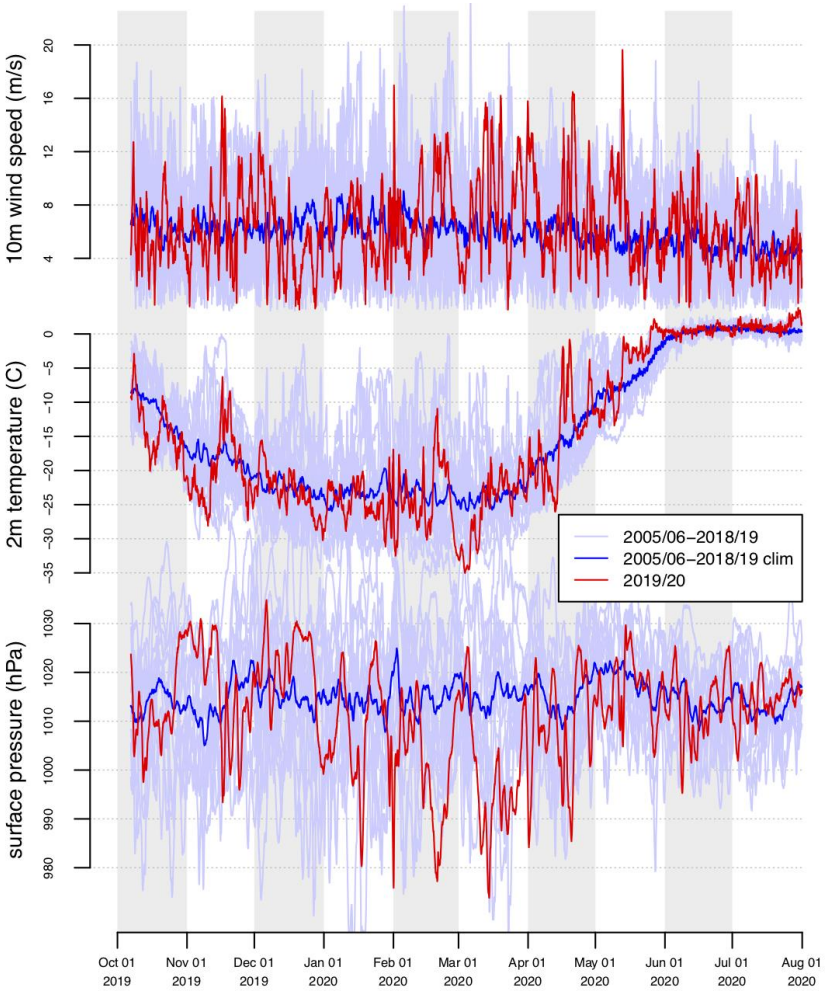

Figure 6: Hourly atmospheric conditions along the MOSAiC drift trajectory according to ERA5 in 2019/2020 (red) and in the preceding 14 years (light blue; average in dark blue). Top: 10 m wind speed; Middle: 2 m temperature; Bottom: surface pressure. See Fig. 7 for a comparison with corresponding ship observations.

665

https://doi.org/10.5194/tc-2021-80
Preprint. Discussion started: 8 April 2021
© Author(s) 2021. CC BY 4.0 License.

The Cryosphere
Discussions
Open Access
EGU

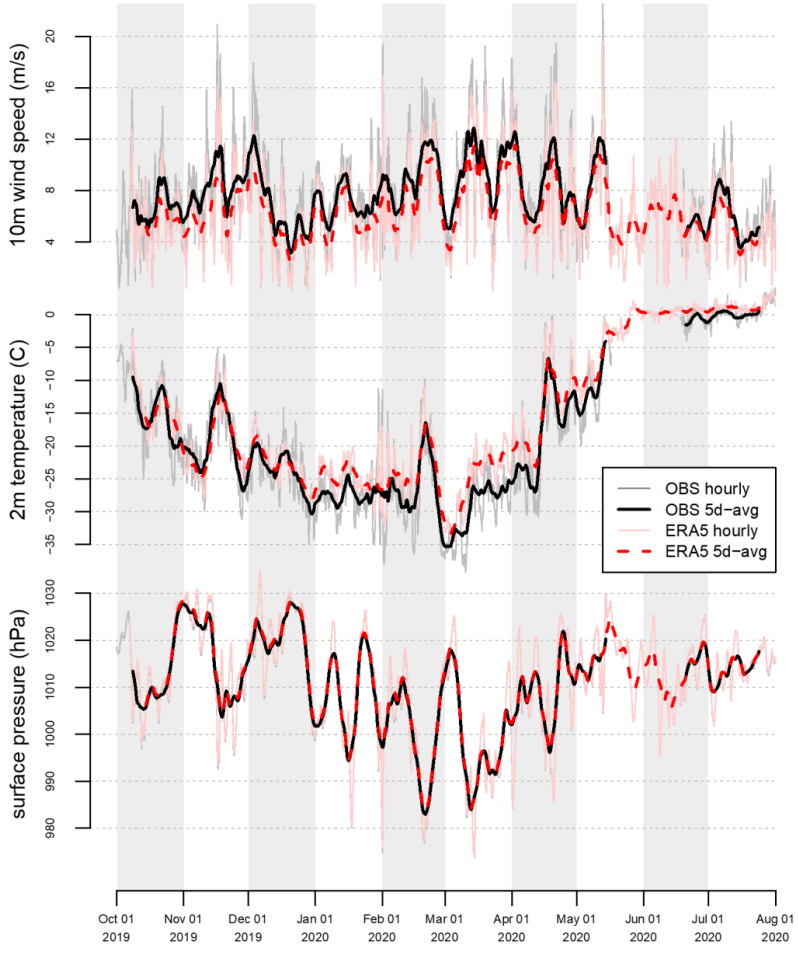

Figure 7: Atmospheric conditions along the MOSAiC drift trajectory in 2019/20 according to ERA5 (red and light red) and according to ship measurements (black and grey). Hourly data are depicted in light red and grey; 5-days-averages are depicted in red (dashed) and black. Top: 10 m wind speed; Middle: 2 m temperature; Bottom: surface pressure.

670

https://doi.org/10.5194/tc-2021-80
Preprint. Discussion started: 8 April 2021
© Author(s) 2021. CC BY 4.0 License.

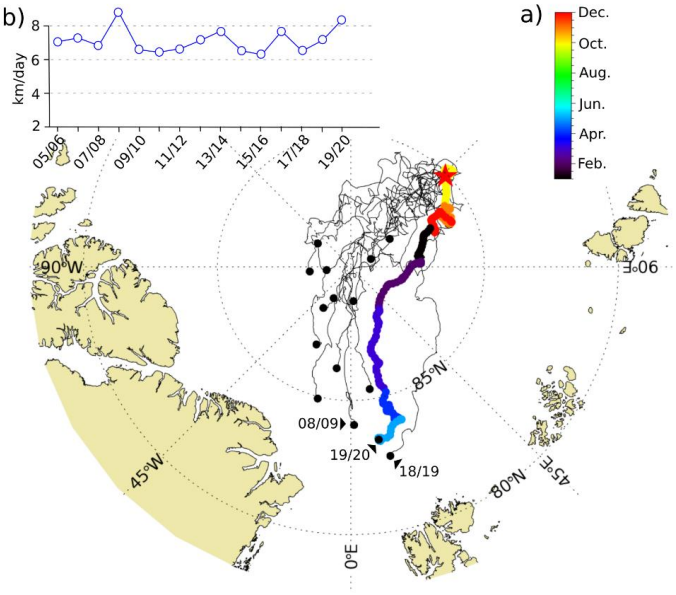

Figure 8: A comparison of the MOSAiC drift with the drift of previous years. a) Results from a forward tracking experiment: Sea ice was traced 14 times in a forward direction for a period of 250 days starting on October 4 (2005 – 2019) from the position where *Polarstern* was moored to the floe (red star). The multicoloured trajectory line, with colours corresponding to the month of year, indicates the reproduced drift of the MOSAiC CO (Central Observatory). All other years (2005 – 2018) are shown as black lines. The end nodes of the individual tracks are marked by a black circle. b) Averaged displacement of sea-ice per day (km) for the individual years.

https://doi.org/10.5194/tc-2021-80
Preprint. Discussion started: 8 April 2021
© Author(s) 2021. CC BY 4.0 License.

The Cryosphere Discussions
Open Access
EGU

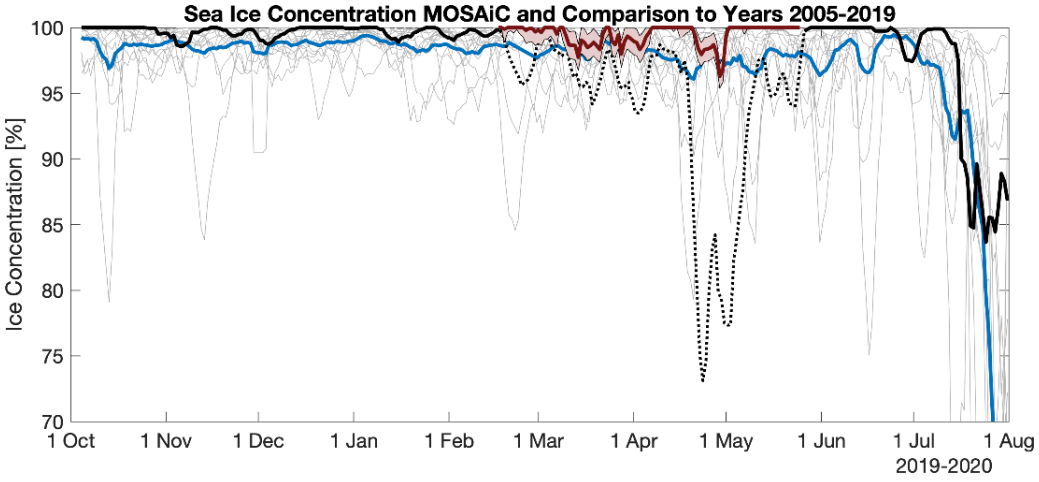

Figure 9: Sea-ice concentration within a 3 km radius around the CO (6.25 km grid cell, black) along the MOSAiC drift from October 4, 2019 to July 31, 2020 in comparison to the ice concentrations from 2005/2006 to 2018/2019 for the same drift trajectory. The blue line shows the average for 2005/2006–2018/2019 while the grey lines show the individual years. All timeseries are smoothed with a 5-day running mean. During spring warm air intrusions with rain on snow caused a significant temporary reduction of the sea-ice concentration (dashed black line). We therefore show in addition an alternative sea-ice concentration data set during that time with uncertainty estimates (red and shaded red; not available for the climatology, see main text).

https://doi.org/10.5194/tc-2021-80
Preprint. Discussion started: 8 April 2021
© Author(s) 2021. CC BY 4.0 License.

The Cryosphere Discussions
Open Access
EGU

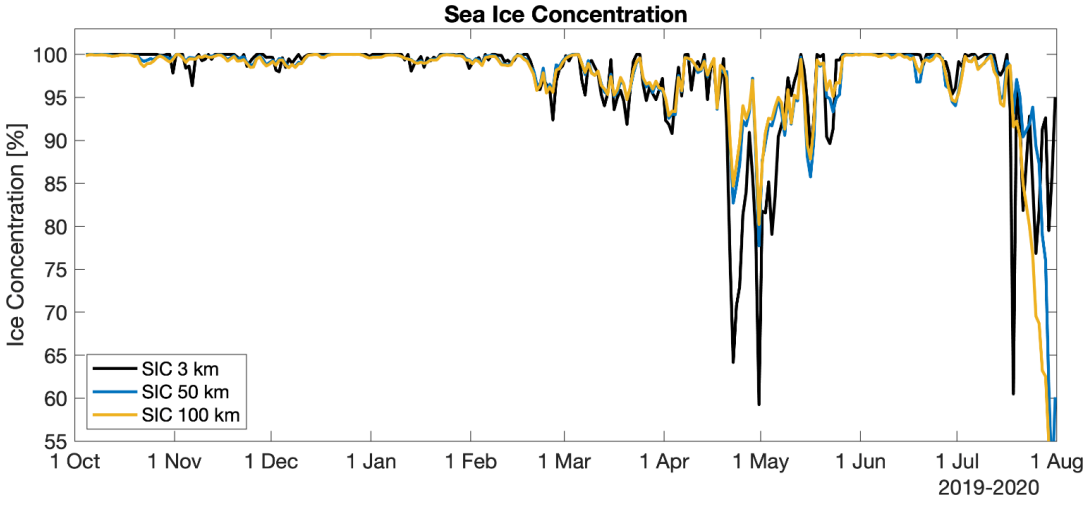

Figure 10: Sea-ice concentration (SIC) along the MOSAiC drift trajectory from the start of the drift on 4th October 2019 until the end of the first floe on July 31 2020. Daily (no smoothing) sea-ice concentrations are shown at 3.125 (black), 50 (blue), and 100 km (yellow) radius. Please mind the significantly underestimated concentrations between mid-April to May and associated discussion in the main text and Figure 5.

https://doi.org/10.5194/tc-2021-80
Preprint. Discussion started: 8 April 2021
© Author(s) 2021. CC BY 4.0 License.

705

Figure 11: Distance of the MOSAiC CO to the ice edge obtained from the sea-ice concentration data set.

https://doi.org/10.5194/tc-2021-80
Preprint. Discussion started: 8 April 2021
© Author(s) 2021. CC BY 4.0 License.

The Cryosphere Discussions
Open Access
EGU

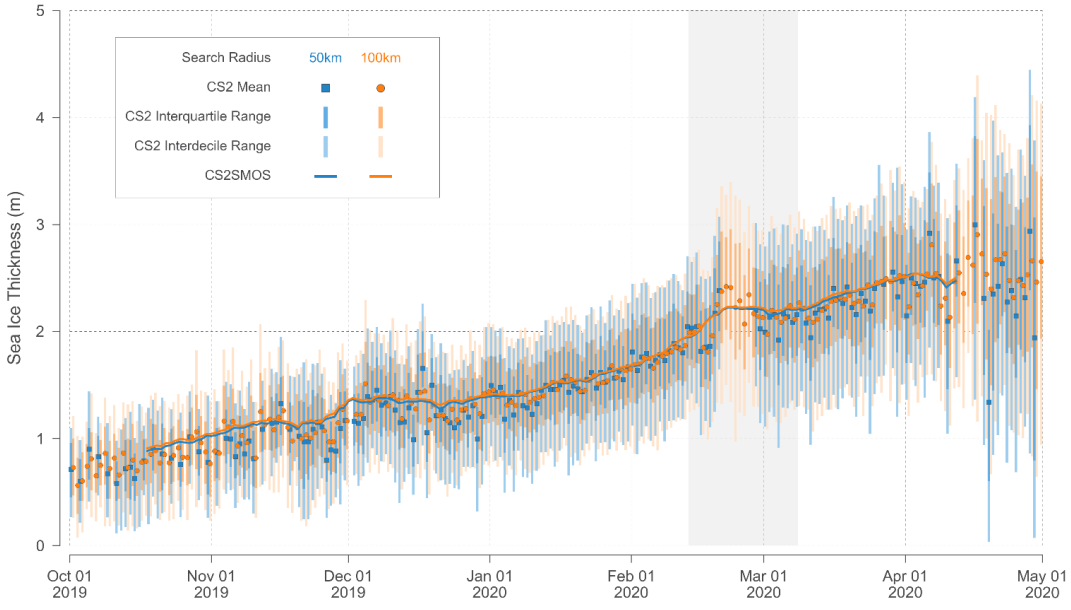

Figure 12: Daily sea-ice thickness estimates from CryoSat-2 (CS2) full resolution orbit L2P data and gridded CryoSat-2/SMOS (CS2SMOS) multi-sensor thickness analysis extracted along the noon position of the CO at two different search radii (50 and 100 km). The grey rectangle indicates when the CO drifted north of 88N and outside the CS2 orbit coverage. The distribution of CS2 orbit data within the search radii is described by the mean value, interquartile (25% to 75% percentiles) and interdecile ranges (10% to 90% percentiles). For CS2SMOS, only the mean values of grid values within the search radius are provided.

https://doi.org/10.5194/tc-2021-80
Preprint. Discussion started: 8 April 2021
© Author(s) 2021. CC BY 4.0 License.

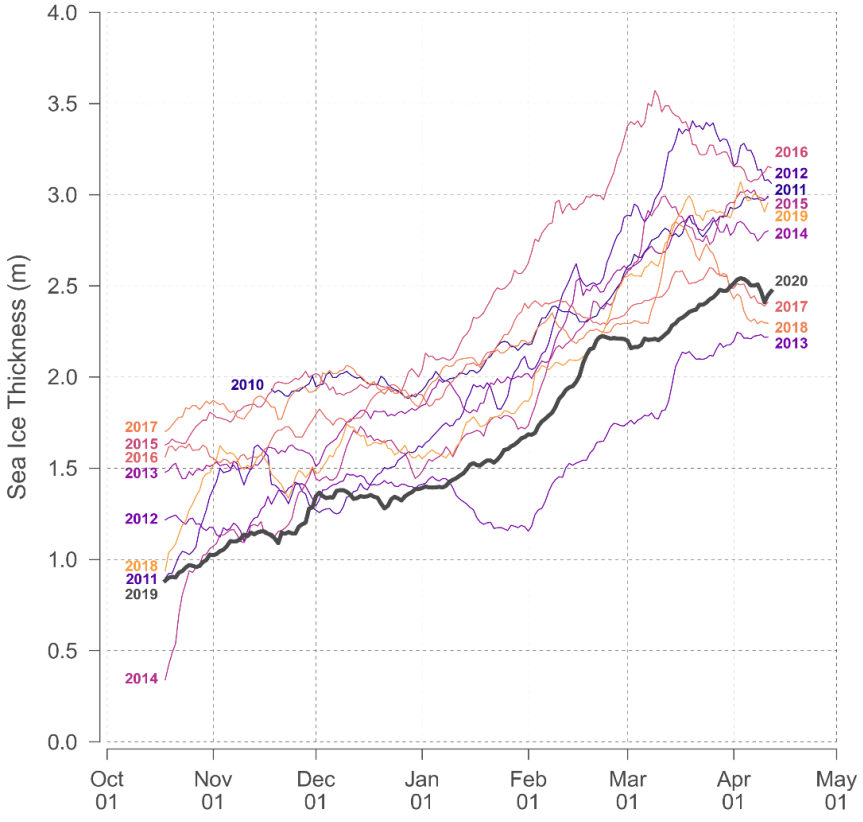

Figure 13: Daily sea-ice thickness from gridded CryoSat-2/SMOS (CS2SMOS) multi-sensor thickness analysis extracted within 50 km of the CO noon position for all Arctic winters in the CS2SMOS data record. Each winter season is marked by the start and end year, e.g. 2011/2012. Bold black line indicates data during the MOSAiC year and is identical to the 50 km radius CS2SMOS data in Fig. 12.

https://doi.org/10.5194/tc-2021-80
Preprint. Discussion started: 8 April 2021
© Author(s) 2021. CC BY 4.0 License.

The Cryosphere Discussions
Open Access
EGU

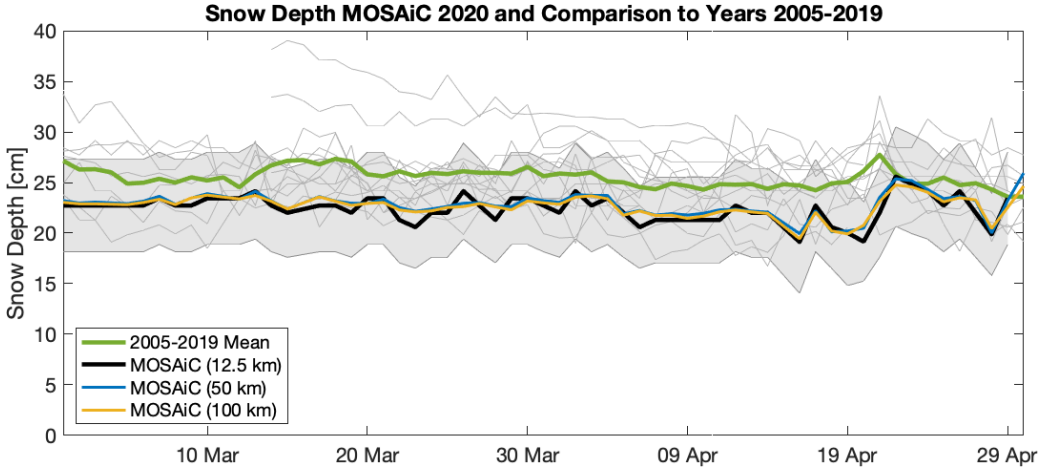

Figure 14: Snow depth from the AMSR-E and AMSR2 satellite microwave radiometers from March 1 to April 30 of the years 2005 to 2020 (without 2012) at the MOSAiC location. For the MOSAiC year 2020 the thick black line shows snow depth at 12.5 km radius. The grey shaded area indicates the corresponding uncertainty bounds (Rostosky et al, 2018, 2020). The blue and yellow line gives the mean snow depth at a 50 and 100 km radius for comparison. The thin grey lines show the individual years 2005 to 2019 and the green line provides the climatological mean. Because the MOSAiC floe was located in an area with partly second year ice, snow depth can only be retrieved for March and April (Rostosky et al, 2018).

https://doi.org/10.5194/tc-2021-80
Preprint. Discussion started: 8 April 2021
© Author(s) 2021. CC BY 4.0 License.

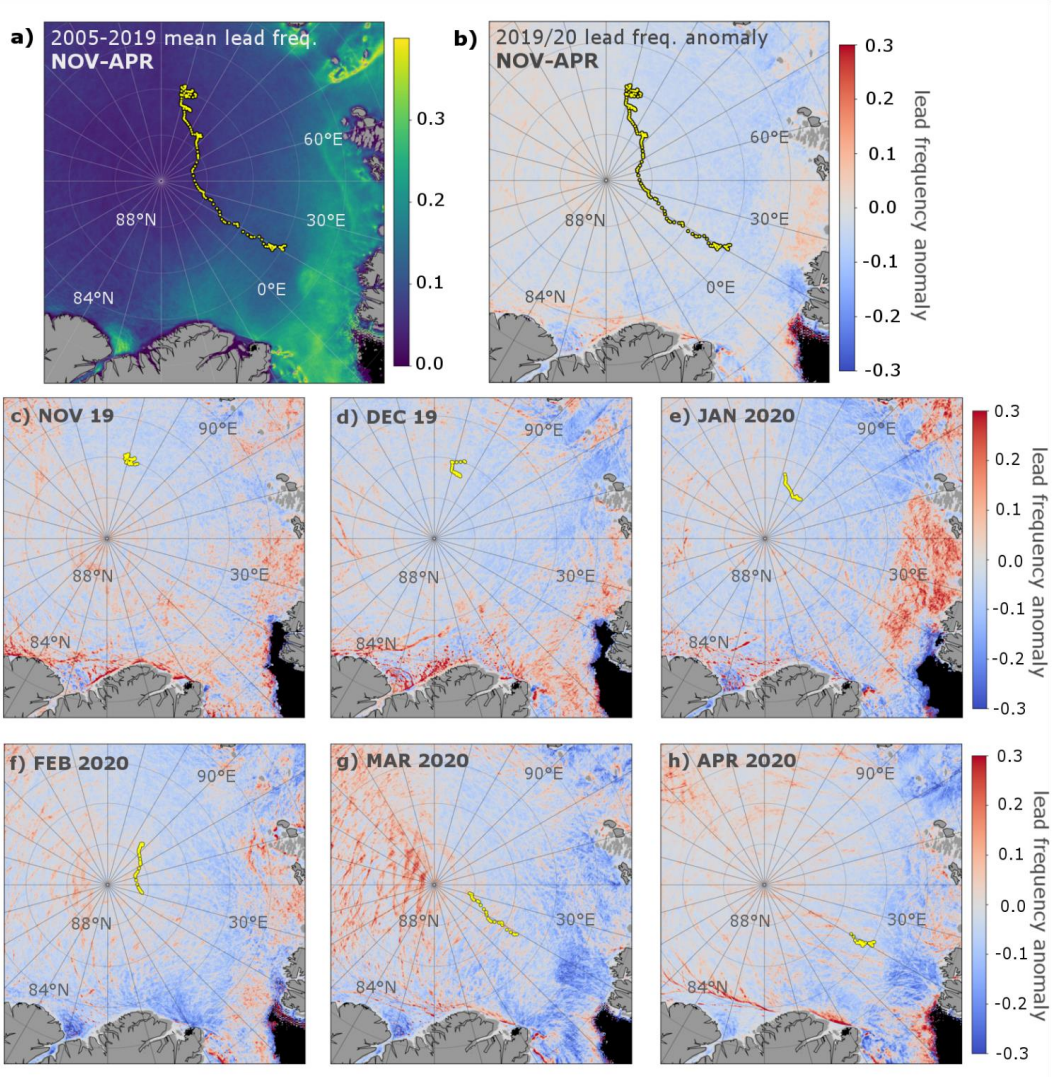

735 **Figure 15**: a) Spatial distribution of the mean frequency of occurrence of sea-ice leads for the months of November to April for the winter seasons 2005/2006 to 2018/2019. MOSAiC drift of the CO is shown by yellow dots; b) lead frequency anomaly for the MOSAiC winter 2019/2020 with respect to the reference period, c-h) monthly lead frequency anomalies for the months of November to April in 2019/2020, respectively.

https://doi.org/10.5194/tc-2021-80
Preprint. Discussion started: 8 April 2021
© Author(s) 2021. CC BY 4.0 License.

The Cryosphere
Discussions
Open Access
EGU

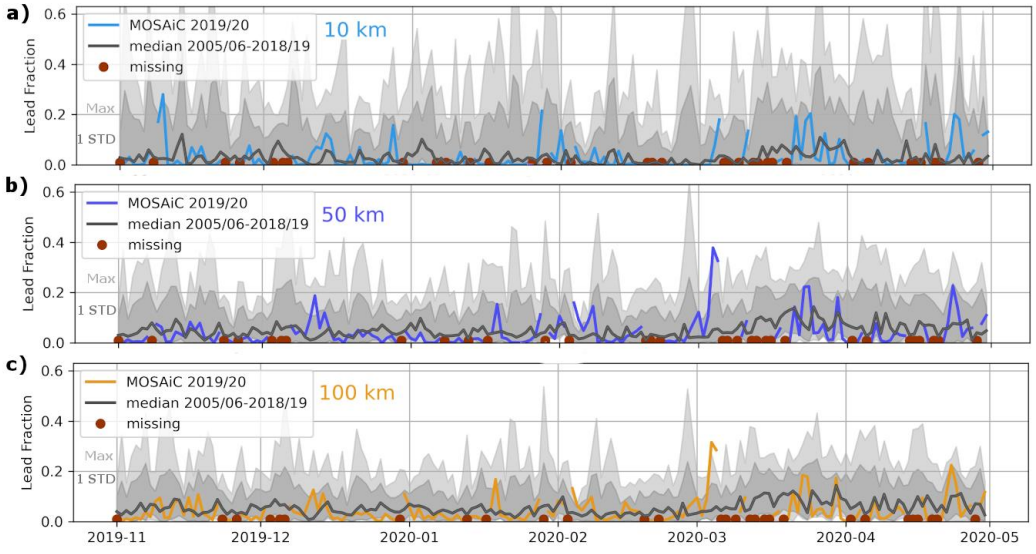

740

Figure 16: Temporal evolution of the lead fraction around the CO during MOSAiC for a) a radius of 10 km (light blue), b) 50 km (dark blue), and c) 100 km (orange), respectively. Maximum (light grey area), mean (black line) and one standard deviation (dark grey area) of lead fraction for the reference period 2005/06 to 2018/19 are shown for comparison.

https://doi.org/10.5194/tc-2021-80
Preprint. Discussion started: 8 April 2021
© Author(s) 2021. CC BY 4.0 License.

745

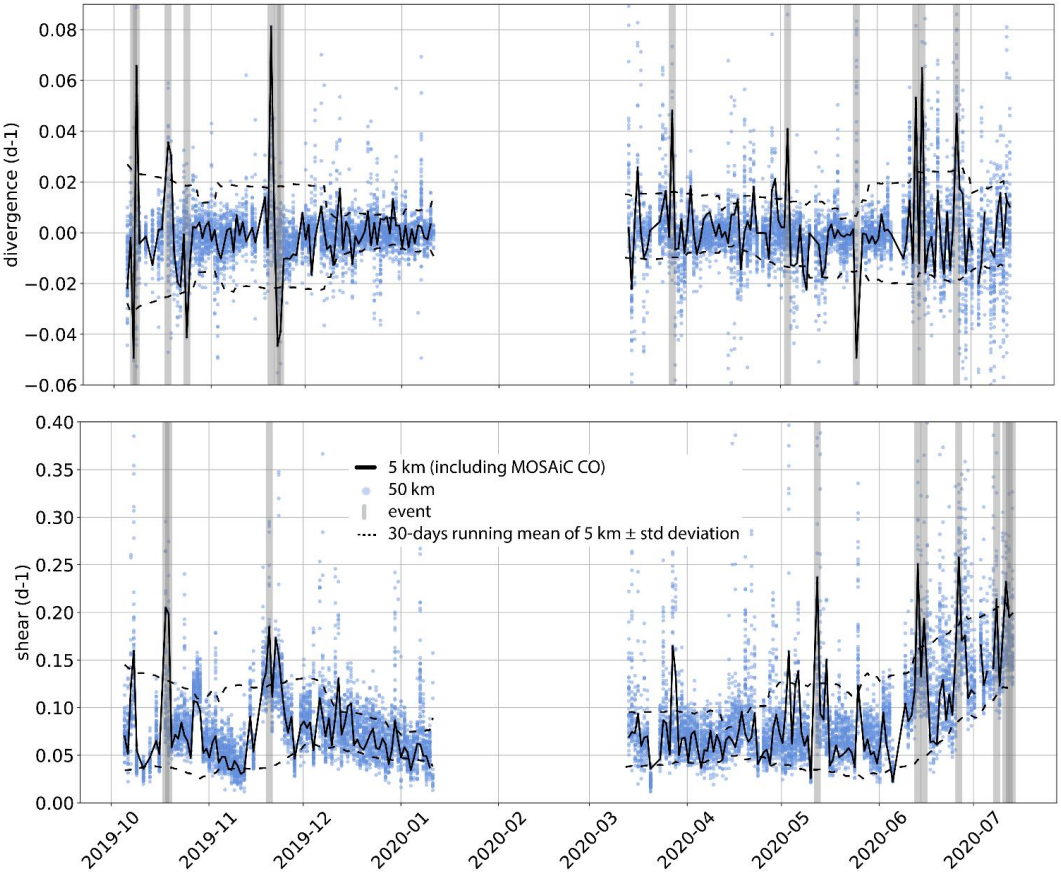

Figure 17: Time series of a) divergence and b) shear extracted from Sentinel-1 SAR scenes along the MOSAiC drift at different radii (5 km in black vs. 50 km in blue, compare Fig. 3) between October 5,2019 and July 14, 2020. Strong deformation events with a magnitude of more than two standard deviations are marked by grey bars. The 30-days running mean ± standard
750 deviation illustrates the seasonal variability.

https://doi.org/10.5194/tc-2021-80
Preprint. Discussion started: 8 April 2021
© Author(s) 2021. CC BY 4.0 License.

The Cryosphere Discussions
Open Access
EGU

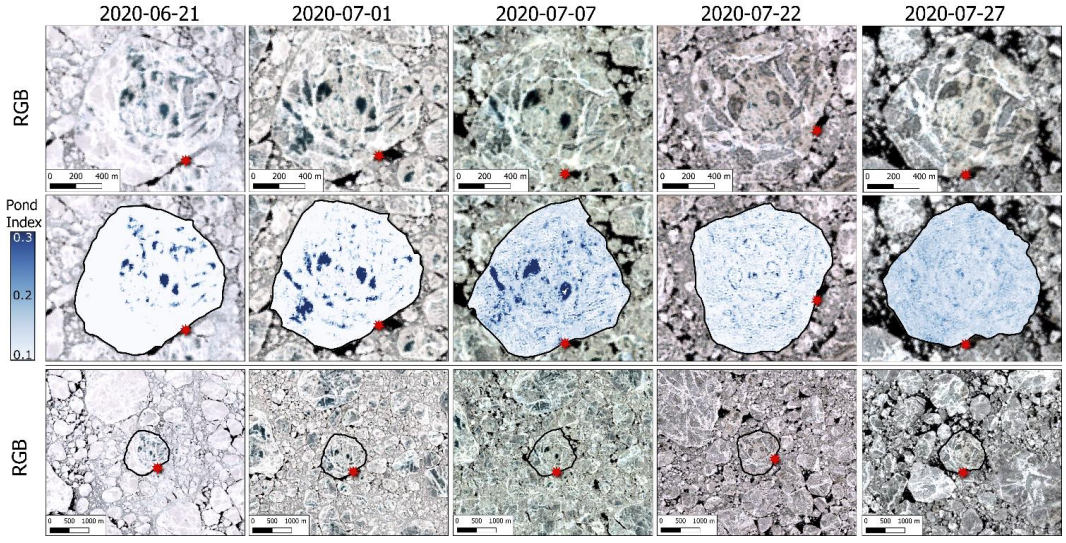

Figure 18: Upper panel: Sentinel-2 MSI True colour images of the MOSAiC floe obtained between 21July 21 and July 27, 2020. Central panel: Outline of the MOSAiC CO (black) and areas with classified melt ponds (pond index). Lower panel: True Colour image showing the larger surrounding of the MOSAiC floe (black outline) and the temporal evolution of melt pond on the surface of neighbouring floes. The Red star shows the position of *Polarstern* at the time of the satellite image acquisition.

https://doi.org/10.5194/tc-2021-80
Preprint. Discussion started: 8 April 2021
© Author(s) 2021. CC BY 4.0 License.

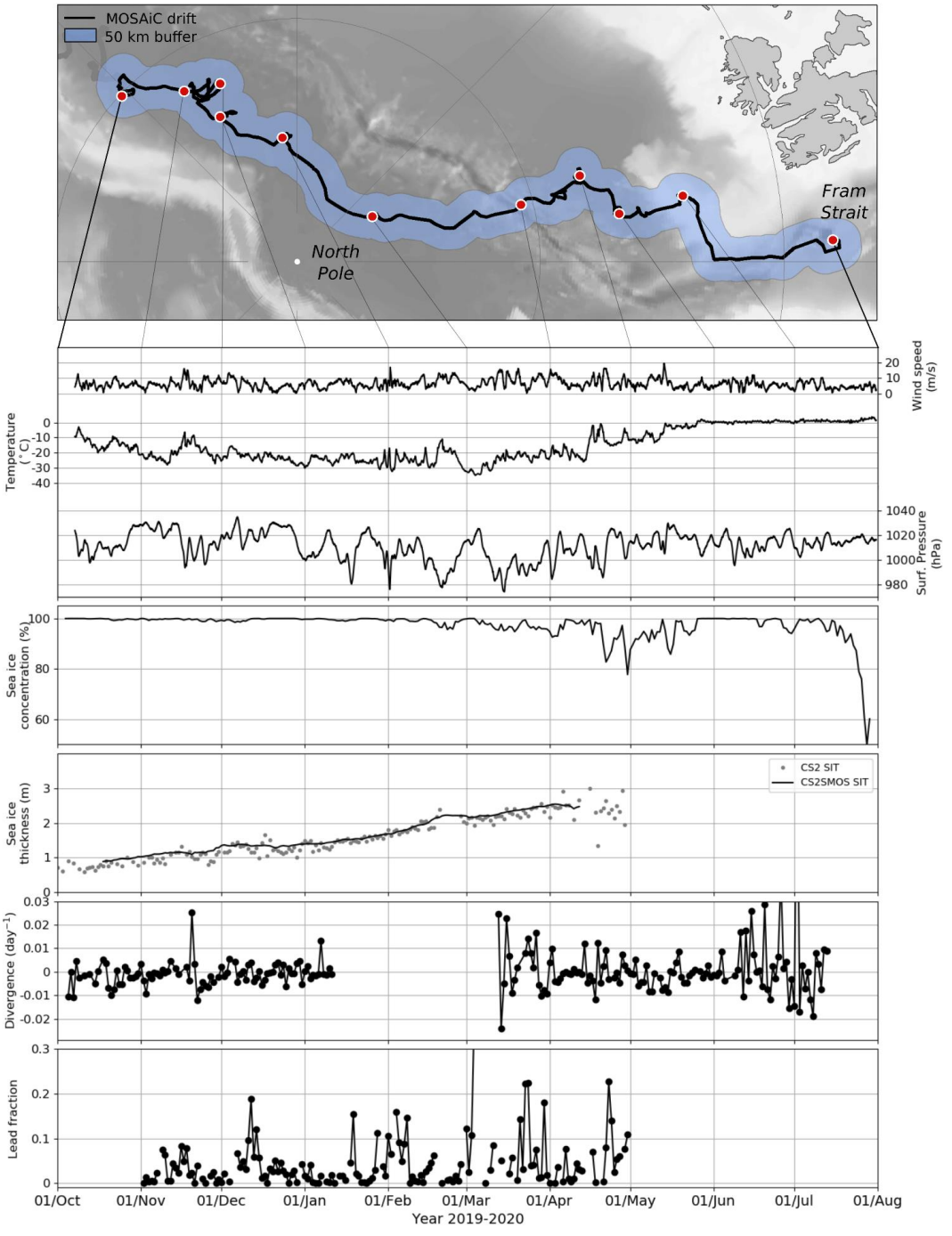

Figure 19: Summary of the atmospheric and ice conditions extracted from reanalysis and satellite data within a 50 km radius (top) along the MOSAiC CO drift track.